Comprehensive Molecular Characterization Identifies Distinct Genomic and Immune Hallmarks of Renal Medullary Carcinoma

Pavlos Msaouel, Gabriel Malouf, Xiaoping Su, Hui Yao, Durga Tripathi, Melinda Soeung, Jianjun Gao, Priya Rao, Cristian Coarfa, Chad Creighton, et al.

HHS Public Access

Author manuscript

Cancer Cell. Author manuscript; available in PMC 2021 May 11.

Published in final edited form as:

Cancer Cell. 2020 May 11; 37(5): 720–734.e13. doi:10.1016/j.ccell.2020.04.002.

Comprehensive Molecular Characterization Identifies Distinct Genomic and Immune Hallmarks of Renal Medullary Carcinoma

Pavlos Msaouel[1,2,19,*], **Gabriel G. Malouf**[3,4], **Xiaoping Su**[5], **Hui Yao**[5], **Durga N. Tripathi**[2], **Melinda Soeung**[6], **Jianjun Gao**[1], **Priya Rao**[7], **Cristian Coarfa**[8], **Chad J. Creighton**[5,8], **Jean-Philippe Bertocchio**[1,2], **Selvi Kunnimalaiyaan**[9], **Asha S. Multani**[10], **Jorge Blando**[11], **Rong He**[1], **Daniel D. Shapiro**[12], **Luigi Perelli**[1], **Sanjana Srinivasan**[6,13], **Federica Carbone**[1], **Patrick G. Pilié**[1], **Menuka Karki**[2], **Riyad N.H. Seervai**[2,14], **Bujamin H. Vokshi**[3,4], **Dolores Lopez-Terrada**[15], **Emily H. Cheng**[16], **Ximing Tang**[17], **Wei Lu**[17], **Ignacio I. Wistuba**[17], **Timothy C. Thompson**[1], **Irwin Davidson**[4], **Virginia Giuliani**[13,18], **Katharina Schlacher**[9], **Alessandro Carugo**[13,18], **Timothy P. Heffernan**[13,18], **Padmanee Sharma**[1,11], **Jose A. Karam**[12,17], **Christopher G. Wood**[12], **Cheryl L. Walker**[2,*], **Giannicola Genovese**[1,6,*], **Nizar M. Tannir**[1,*]

[1]Department of Genitourinary Medical Oncology, The University of Texas MD Anderson Cancer Center, Houston, TX, 77030, USA.

[2]Center for Precision Environmental Health, Baylor college of Medicine, Houston, TX, 77030, USA.

[3]Department of Hematology and Oncology, Strasbourg University Hospitals, Strasbourg University, Strasbourg, France.

[4]Department of Functional Genomics and Cancer, Institut de Génétique et de Biologie Moléculaire et Cellulaire, CNRS/INSERM/UNISTRA, Illkirch Cédex, France

[5]Department of Bioinformatics and Computational Biology, The University of Texas MD Anderson Cancer Center, Houston, TX, 77030, USA.

[*]**Address correspondence to**: Nizar M. Tannir, MD, FACP, Department of Genitourinary Medical Oncology, Unit 1374, The University of Texas MD Anderson Cancer Center, 1155 Pressler St, Houston, TX 77030-3721, Fax: (713) 745-1625, NTannir@mdanderson.org, Giannicola Genovese, MD, Department of Genitourinary Medical Oncology, Unit 1374, The University of Texas MD Anderson Cancer Center, 1155 Pressler St, Houston, TX 77030-3721, Fax: (713) 745-1625, GGenovese@mdanderson.org, Cheryl Lyn Walker, PhD, Center for Precision Environmental Health, Departments of Cellular and Molecular Biology and Medicine, Baylor College of Medicine, Houston, TX 77030, Phone: (713) 798-8193, Fax: (713) 798-8181, Cheryl.Walker@bcm.edu, Pavlos Msaouel, MD, PhD, Department of Genitourinary Medical Oncology, Unit 1374, The University of Texas MD Anderson Cancer Center, 1155 Pressler St, Houston, TX 77030-3721, Fax: (713) 745-7575, PMsaouel@mdanderson.org.

Author Contributions

Conceptualization, P.M., G.G.M, C.L.W, G.G, N.M.T.; Methodology, P.M., G.G.M., X.S., H.Y., D.N.T., J.J.G., C.C., C.J.C., P.G.P., M.S., S.S., J.P.B., D.D.S., R.N.H.S., S.K., K.S., B.H.V., C.L.W., G.G., N.M.T.; Formal Analysis, P.M., G.G.M., X.S., H.Y., D.N.T., C.C., C.J.C., M.S., S.S., J.P.B., D.D.S., R.N.H.S., S.K., K.S.; Investigation, P.M., G.G.M., D.N.T., P.R., A.S.M., X.T., I.I.W., R.H., M.S., L.P., J.P.B., D.D.S., M.K., R.N.H.S., B.H.V., D.L.T., W.L., V.G., A.C., T.P.H., P.S., J.A.K., C.G.W., C.L.W., G.G., N.M.T.; Writing - Original Draft, P.M., G.G., C.L.W; Writing - Review and Editing, P.M., G.G.M., X.S., H.Y., D.N.T., J.J.G., P.R., C.C., C.J.C., A.S.M., J.B., D.D.S., M.S., L.P., S.S., J.P.B., P.G.P., R.N.H.S., D.L.T., I.I.W., V.G., A.C., T.P.H., P.S., J.A.K., C.G.W., C.L.W., G.G., N.M.T.; Resources, P.M., G.G.M., X.S., H.Y., D.N.T., C.C., C.J.C., A.S.M., J.B., R.H., M.S., L.P., J.P.B., D.D.S., F.C., M.K., R.N.H.S., D.L.T., E.H.C., X.T., W.L., I.I.W., T.C.T., I.D., V.G., A.C., T.P.H., P.S., C.L.W., G.G., N.M.T.; Supervision, P.M., C.L.W., G.G., N.M.T.; Funding Acquisition, P.M., C.L.W., G.G., N.M.T.

Declaration of Interests: The authors declare no competing interests.

[6]Department of Genomic Medicine, The University of Texas M.D. Anderson Cancer Center, Houston, TX, 77030, USA.

[7]Department of Pathology, The University of Texas M.D. Anderson Cancer Center, Houston, TX, 77030, USA.

[8]Department of Medicine and Dan L. Duncan Cancer Center, Baylor College of Medicine, Houston, TX, 77030, USA.

[9]Department of Cancer Biology, University of Texas MD Anderson Cancer Center, Houston, TX, 77030, USA.

[10]Department of Genetics, The University of Texas M.D. Anderson Cancer Center, Houston, TX, 77030, USA.

[11]Department of Immunology, The University of Texas M.D. Anderson Cancer Center, Houston, TX, 77030, USA.

[12]Department of Urology, The University of Texas M.D. Anderson Cancer Center, Houston, TX, 77030, USA.

[13]Institute for Applied Cancer Science, The University of Texas MD Anderson Cancer Center, Houston, TX, 77030, USA.

[14]Molecular & Cellular Biology Graduate Program; Medical Scientist Training Program, Baylor College of Medicine, Houston, TX, 77030, USA.

[15]Department of Pathology, Texas Children's Hospital, Houston, TX, 77030, USA.

[16]Human Oncology & Pathogenesis Program and Department of Pathology, Memorial Sloan Kettering Cancer Institute, New York City, NY, 10065, USA.

[17]Department of Translational Molecular Pathology, The University of Texas M.D. Anderson Cancer Center, Houston, TX, 77030, USA.

[18]Translational Research to Advance Therapeutics and Innovation in Oncology (TRACTION), The University of Texas MD Anderson Cancer Center, Houston, TX, 77030, USA.

[19]Lead Contact

SUMMARY

Renal medullary carcinoma (RMC) is a highly lethal malignancy that mainly afflicts young individuals of African descent and is resistant to all targeted agents used to treat other renal cell carcinomas. Comprehensive genomic and transcriptomic profiling of untreated primary RMC tissues was performed to elucidate the molecular landscape of these tumors. We found that RMC was characterized by high replication stress and an abundance of focal copy number alterations associated with activation of the stimulator of the cyclic GMP-AMP synthase interferon genes (cGAS-STING) innate immune pathway. Replication stress conferred a therapeutic vulnerability to drugs targeting DNA damage repair pathways. Elucidation of these previously unknown RMC hallmarks paves the way to new clinical trials for this rare but highly lethal malignancy.

Graphical Abstract

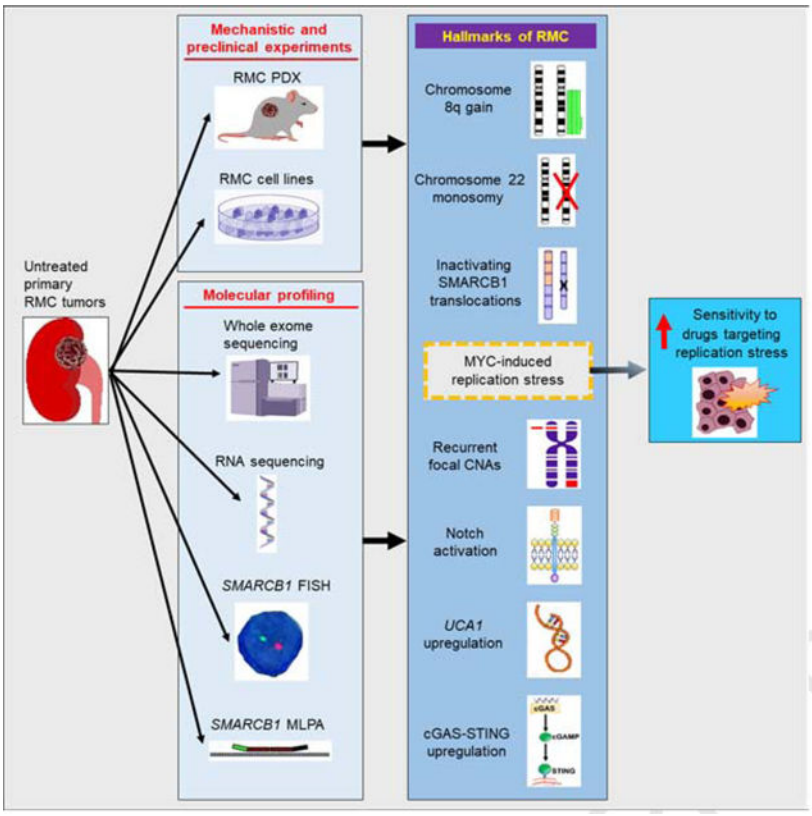

Msaouel et al. describe the molecular landscape of renal medullary carcinomas (RMC). These tumors harbor SMARCB1 mutations leading to high MYC expression and replicative stress that sensitize RMC cells to PARP inhibitors. cGAS-STING activation in RMCs grants exploring immunotherapy for these patients.

Keywords

Molecular profiling; renal medullary carcinoma; replication stress; SMARCB1; cGAS-STING pathway

INTRODUCTION

Although relatively rare, renal medullary carcinoma (RMC) is the third most common kidney malignancy among adolescents and young adults (Cajaiba et al., 2018). It is uniformly associated with sickle hemoglobinopathies (Msaouel et al., 2018) and most frequently occurs in young males of African descent at a median age of 28 years old (Msaouel et al., 2019; Shah et al., 2017). RMC is resistant to all targeted therapies commonly used against other renal cell carcinomas and is highly aggressive with < 5% of patients surviving longer than 36 months (Msaouel et al., 2019). In addition, the best available cytotoxic chemotherapy regimens produce a, typically brief, objective response in only 29% of RMC cases (Msaouel et al., 2019; Shah et al., 2017). Consequently, effective treatment strategies are urgently needed for this lethal disease, a need that is difficult to

address given the dearth of knowledge regarding the molecular landscape of this rare malignancy.

All RMC tumors are characterized by loss, as determined by immunohistochemistry, of the potent tumor suppressor SMARCB1, alternatively known as INI1, hSNF5, or BAF47. SMARCB1 is a subunit of the SWItch/Sucrose Non-Fermentable (SWI/SNF) complex, which hydrolyzes ATP to remodel chromatin structure. Inactivation of SMARCB1 deregulates the activity of SWI/SNF, resulting in aggressive tumors (Kadoch and Crabtree, 2015). In addition to RMC, inactivation of SMARCB1 occurs in the majority of malignant rhabdoid tumors (MRT), atypical teratoid/rhabdoid tumors (ATRT), and epithelioid sarcomas (ES) (Fuller, 2016).

RMC occurs in approximately 1/20,000 individuals with sickle cell trait (Alvarez et al., 2015; Msaouel et al., 2018). To meet the need for new therapies for this disease, we established and molecularly profiled a multi-institutional patient cohort of previously untreated primary RMC tumor samples.

RESULTS

The Mutational Landscape of RMC Distinguishes It from Other Renal Cell Carcinomas

As is typical of RMC (Alvarez et al., 2015; Shah et al., 2017), the majority of our cases (68.4%) arose from the right kidney, the median age at diagnosis was 28 years old, 73.7% of patients were men, 65.8% had metastatic stage IV disease at diagnosis, and only 34.2% had an objective, albeit temporary, response to cytotoxic chemotherapy (Figure 1). All RMC samples were confirmed to be SMARCB1 negative by immunohistochemistry (Figure S1A). Overall, rates of single nucleotide variants (SNVs) and insertion and deletion mutations (inDels) were very low for RMC. Whole exome sequencing (WES) landscapes for 31 untreated primary tumor samples and 15 matched normal samples were used to determine SNVs and inDels, with an average mean target sequencing coverage of 73-fold for tumor tissue and 60-fold for matched normal tissue, and a mean estimated tumor purity of 49.1% (range, 24%–98%). A total of 1332 SNVs and inDels in 1165 genes were identified by WES, with a median of 24 per patient (Figure 1 and Supplementary Table 1). Clinical targeted next-generation sequencing of 5/31 untreated primary tumor samples (Figure 1) did not detect additional SNVs and inDels. In two additional patient samples (RMC20T and RMC27T) for which no tissue was available to reliably perform WES, targeted next-generation sequencing by FoundationOne CDx did not detect any mutations. The low non-synonymous mutation load of RMC was similar to that of MRT (which is also characterized by loss of SMARCB1) and lower than most of the tumors sequenced by The Cancer Genome Atlas (TCGA), including other renal cell carcinomas (Figure 2A).

Of the 1165 genes mutated in untreated primary RMC tumors from a total of 31 patients, only 22 were known tumor suppressors or oncogenes listed in the Catalogue of Somatic Mutations in Cancer (COSMIC) database (Forbes et al., 2017) (Figure S1B and Supplementary Table 1). An additional 10 genes were previously identified as splicing factors linked to other cancer types (Seiler et al., 2018) (Figure S1B and Supplementary Table 1). Figure S1C shows the mutational signature patterns of RMC samples compared

with matched normal samples. The protein classes encoded by the 1165 genes were determined using the PANTHER classification system (Mi et al., 2013) (Figure S1D and Supplementary Table 1). *SETD2* was mutated in 2/31 (6.5%) of RMC tumors and was the only established gene driver of other renal cell carcinomas (Brugarolas, 2014) to be altered in RMC (Figure 1 and Supplementary Table 1).

RMC is Characterized by 8q Gain and Focal Chromosomal Alterations

SMARCB1 is located on chromosome 22, which was lost in 40% of RMC tumors (Figure 2B). Whereas other SMARCB1-deficient malignancies, such as the rhabdoid tumors MRT and ATRT, harbor a simple genome with very few CNAs other than 22q11.23 loss (Chun et al., 2016; Hasselblatt et al., 2013; Lee et al., 2012)(Figure S1E), RMC had recurrent focal chromosomal amplifications and deletions in addition to 22q11.23 loss (Figures 2C, 2D, and S2). Our analysis of previously published WES from MRT and ATRT samples (Lee et al., 2012) revealed a much lower number of focal CNAs (Figure 2E) compared with RMC (Figure 2D). Chromosome 8q gain was noted in 46.7% of RMC tumors, and 21.1% of genes in that chromosome arm were significantly upregulated (FDR < 0.1) per RNA-seq in RMC tumors compared with adjacent normal kidney (Supplementary Table 2). None of the MRT and ATRT tumors harbored an 8q gain (Figure S1E). The genome plots of all seven RMC samples harboring 8q gain are shown in Figure S2. No other recurrent whole or arm-level chromosome gains or losses were found, and approximately half of all RMC tumors (46.2%) were diploid (Figures 2C and S2). Significant focal copy number changes as quantified by GISTIC analysis are shown in Figure 2D, including recurrent deletions in and around the *SMARCB1* locus (22q11.23). Using previously published genomic coordinates (Durkin and Glover, 2007; Kumar et al., 2019), we found that 32.5% of recurrent CNAs in RMC tissues were in chromosomal fragile sites (Supplementary Table 2), suggesting that these alterations are not randomly distributed across the genome. To investigate the biological role of the recurrent focal CNAs found in RMC (Supplementary Table 2) we performed Gene Ontology (GO) analysis, which revealed that genes within the recurrent focal CNAs were enriched for GO terms (Figure 2F) related to histone deacetylation ($p < 0.001$), lipid metabolism and biosynthesis ($p = 0.024$), response to ammonium ions and acetylcholine ($p = 0.024$), DNA transcription ($p = 0.028$), and cytoskeleton-dependent cytokinesis ($p = 0.031$).

The most common focal deletion in both RMC and rhabdoid tumors was in the *SMARCB1* locus 22q11.23 found in 9/15 (60%) RMC tumors and in 28/35 (80%) rhabdoid tumors. In contrast to RMC, focal amplifications were rare in rhabdoid tumors (Figure 2E) and none were found in more than 15% of rhabdoid tumors. The most common focal amplification, found in 9/15 (60%) RMC tumors, was in the 11q14.3 region (Supplementary Table 2). Furthermore, we found amplification of *NOTCH2* in 6/15 (40%) RMC tumors, with 4/15 (26.7%) demonstrating concurrent deletion of *NOTCH1* and *NOTCH3* and amplification of *NOTCH2*, a distinct pattern also found in the basal subtype of bladder urothelial carcinoma (BLCA) and associated with increased cell-cycle progression and epithelial-mesenchymal transition (EMT) (Hayashi et al., 2016). Our transcriptomic analysis (see below) further revealed significant upregulation of genes associated with the Notch pathway in RMC compared with adjacent normal kidney (Figures S3A) and with kidney MRT (Figure S3B). By integrating our genomic and RNA-seq data we identified 341 genes (Supplementary

Table 2) in areas of recurrent focal copy number gain or loss that were significantly (FDR < 0.1) upregulated or downregulated, respectively, in RMC tumors compared with adjacent normal kidney. The reliability of our CNA analyses of WES data was confirmed in sample MED1T by array CGH (Figure 3A), which detected the presence of the focal amplification on chromosome 2p, large amplification of chromosome 8, monosomy of chromosomes 4 and 22, large deletions of chromosomes 15 and 16, and a focal deletion of chromosome 17p13.1 (*TP53* gene region), which were also found by WES (Figure S2).

Structural alterations such as recurrent loss of chromosome 22 (Figure 2B) and focal deletions of the *SMARCB1* locus 22q11.23 (Figure 2D) were far more common than *SMARCB1* SNVs (Figure 1). To further elucidate the molecular events leading to SMARCB1 loss in RMC, we employed a combination of fluorescence *in situ* hybridization (FISH), exome DNA sequencing (WES and targeted sequencing), and multiplex ligation-dependent probe amplification (MLPA) in untreated primary RMC tumor samples (Figures 1, 3B, 3C, and 3D; Supplementary Table 3). Using this comprehensive approach, we identified a genetic *SMARCB1* loss in 32/38 (84.2%) patients with RMC (Figure 1). The most common molecular alteration, noted in 20/38 cases (52.6%), was inactivating translocation of one *SMARCB1* allele and deletion of the second allele. Less frequent were deletion of both *SMARCB1* alleles (6/38 patients; 15.8%), deletion of one *SMARCB1* allele and inDel of the second *SMARCB1* allele (5/38 patients; 13.2%), and deletion of one *SMARCB1* allele and truncating nonsense mutation of the second *SMARCB1* allele (1/38 patients; 2.6%). These results are consistent with two previous studies in a total of 25 patients with RMC that found *SMARCB1* to be inactivated via translocation combined with hemizygous deletion in 15/25 (60%) cases and by homozygous deletions in 7/25 (28%) cases (Calderaro et al., 2016; Carlo et al., 2017; Jia et al., 2019). In addition, we determined that this pattern for *SMARCB1* inactivation (inactivating translocation combined with hemizygous deletion) occurred not only in primary tumors but also in lymph node and liver mestastases of patients RMC38 and RMC32, respectively. Sanger sequencing confirmed that both the primary kidney tumor and the liver metastasis of patient RMC32 harbored the same translocation between the *SMARCB1* and *MYOM1* genes (Figures 3E and 3F). We performed DNA methylation analysis in 3 out of the 4 RMC samples that had no detectable genetic SMARCB1 loss (Figure 1) and found no evidence of increased methylation in and around the *SMARCB1* promoter (Supplementary Table 3). Of note, due to lack of available tissue, these four RMC samples did not undergo multiplatform interrogation by all three assays (WES, FISH, and MLPA), and a potential genetic cause of SMARCB1 loss may thus have been missed.

RNA-seq (see below) of 5 samples (RMC32T, RMC36T1, MED1T, MED2T, MED5T) that harbored inactivating translocations identified *SMARCB1* fusion transcripts in 2/5 cases (RMC32T and MED1T) as shown in Figure 3E. Both of the *SMARCB1* fusion products are predicted to be functionally inactive as they lack all of the known protein interaction domains of this member of the SWI/SNF complex (Figure 3G). Additionally, we interrogated our RNA-seq data for evidence of infection by oncogenic human viruses (complete list in the STAR Methods section) and detected no viral genomes in any RMC samples, indicating that viral genomic integration did not contribute to RMC pathogenesis.

Transcriptomic Signature Distinguishes RMC from Other Renal Malignancies

We compared the protein-coding and long non-coding RNA (lncRNA) gene expression profiles of eleven untreated primary RMC tumors to other malignancies arising in or near the renal medulla: CDC and UTUC. As shown in the heat map in Figure 4A, RMC harbored a distinct signature that clustered more closely to CDC than to UTUC (Figures 4A and S3C. The RMC36T1 sample that clustered within the CDC samples in our unsupervised analysis of protein-coding gene expression (Figure 4A) was confirmed to be RMC as the patient had sickle cell trait by hemoglobin electrophoresis (Figure 1) and the tumor was negative for SMARCB1 by immunohistochemistry (Figure S1A). Additional comparisons with other cancers arising from the kidney (Figures 4B and S3D) again confirmed that RMC is most closely related to CDC and is clearly distinct from kidney MRT, the second most common SMARCB1-deficient malignancy arising from the kidney. Notably, all five renal cell carcinomas formed a separate cluster from kidney MRT (Figures 4B and S3D), consistent with the distinct morphological appearance of kidney MRT from carcinomas (Pawel, 2018).

The distinct gene expression profiles of RMC compared with kidney MRT, despite their common renal origin and shared etiology of SMARCB1 inactivation, led us to explore the nephron site of origin of these malignancies. Using an external gene expression data-set of normal tissue microdissected from various nephron regions (Cheval et al., 2012), the gene expression profiles of RMC, CDC, ccRCC, papillary renal cell carcinoma (PRCC), chromophobe renal cell carcinoma (ChRCC), and kidney MRT were globally compared by supervised analysis with that of each sample in the nephron atlas (Figure 4C). RMC mRNA expression demonstrates a high degree of correlation with the collecting duct, which is also the putative site of origin for CDC, whereas there was no correlation between the transcriptome of kidney MRT and the collecting duct, suggesting that RMC and kidney MRT have a different origin in the nephron (Figure 4C). As expected (Young et al., 2018), the transcriptomes of ccRCC and PRCC indicate an origin from more proximal (cortical) regions of the nephron.

Supplementary Table 4 lists the protein-coding genes differentially expressed between untreated primary RMC tumors samples (n = 11 cases) and adjacent control kidney (n = 6 cases). We noted that genes associated with replication stress and innate immune responses were predominantly upregulated in RMC compared with normal kidney (Figure 4D). This was confirmed by GSEA analysis, which revealed that biological pathways upregulated in untreated primary RMC compared with adjacent normal kidney were enriched for genes involved in inflammatory/immune responses, DNA repair, and c-MYC signaling (Figure S3E). Several metabolic pathways were downregulated in RMC (Figure S3E), and Figure 4E shows a metabolic pathway diagram of the individual genes altered in RMC compared with adjacent normal kidney. Genes related to the tricarboxylic acid (TCA) cycle and oxidative phosphorylation were decreased in RMC, whereas genes involved in fatty acid synthesis were increased. Interestingly, given the hypoxic nature of the renal medulla, RMC displayed increased expression of genes associated with hypoxia and hypoxia-induced EMT (Figure 4F). RMC and CDC demonstrated similar core metabolic and hypoxia-associated gene expression patterns (Figures S4A and S4B). Conversely, when comparing RMC with MRT, genes related to the TCA cycle and fatty acid synthesis were upregulated in RMC, whereas

genes involved in oxidative phosphorylation were downregulated in RMC (Figures S4C and S4D).

In addition to protein-coding genes, we identified lncRNAs differentially expressed between RMC and normal kidney (Figure S4E and Supplementary Table 4). The highest upregulated lncRNA was *urothelial cancer associated 1* (*UCA1*), which showed a 305-fold increase in RMC tumors. *UCA1* is also dramatically upregulated in urothelial carcinoma and was previously considered to be highly specific for urothelial carcinoma (Wang et al., 2006). *UCA1* levels in RMC tumors were similar to those in UTUC and significantly higher than in CDC or other carcinomas of the kidney (Figure S4F). Four other lncRNAs previously shown to be associated with cancer (Arun et al., 2018) were upregulated in RMC: *GAS5*, *HOTAIR*, *PVT1*, and *H19*. There was no copy number gain noted at the genomic loci of the five cancer-associated lncRNAs upregulated in RMC (Supplementary Table 2).

RMC Has a Distinct Immune Profile

The inflammatory/immune response gene expression signature of RMC led us to next characterize the immune cell infiltration of these tumors. Deconvolution of tissue-infiltrating immune and stromal populations revealed that RMC harbored an abudance of fibroblasts (Figure 5A and Supplementary Table 5) consistent with the prominent stromal desmoplasia that is characteristic of this tumor (Gupta et al., 2012). Notably, the abundance of stromal cells in the tumor microenvironment of RMC was similar to that of CDC and very distinct from kidney MRT (Figure S5A). RMC had a paucity of endothelial cells relative to ccRCC (Figure 5A), consistent with the prominent angiogenesis induced by VHL loss in ccRCC (Choueiri and Motzer, 2017).

RMC contains a similarly high number of T cells and cytotoxic lymphocytes compared to those of ccRCC (Figure 5A), a kidney malignancy known to be susceptible to immune checkpoint therapies (Choueiri and Motzer, 2017). However, in contrast to ccRCC, RMC tumors harbor an abundance of myeloid dendritic cells, neutrophils, and B lineage cells (Figure 5A). Immune suppression can involve multiple immune checkpoints, many of which were found to be upregulated in RMC tissues which showed increased expression of immune checkpoint receptors such as PD-1, CTLA-4, and LAG3 (Figure 5B). We validated these transcriptomic findings by immunohistochemistry (IHC), which confirmed that RMC tissues contain high levels of $CD3^+$ T cell lymphocytes, $CD4^+$ helper T cells, $CD8^+$ cytotoxic T cells, $FOXP3^+$ regulatory T cells, $CD68^+$ macrophages, $CD20^+$ B cell lymphocytes, and the PD-1 immune checkpoint, whereas the staining pattern of the PD-L1 immune checkpoint was heterogeneous with some RMC tumors demonstrating increased PD-L1 expression on both tumor cells and surrounding immune cells (Figures 5C, S5B, S5C, S5D, and Supplementary Table 5).

Focal CNAs such as deletions, duplications, and translocations are associated with increased cytosolic DNA leakage leading to upregulation of the cyclic GMP-AMP synthase-stimulator of interferon genes (cGAS-STING) cytosolic double-stranded DNA-sensing anti-viral innate immune pathway (Bakhoum et al., 2018; Tijhuis et al., 2019). Accordingly, in regard to the differential gene expression between RMC and normal kidney (Supplementary Table 4), we noted upregulation of the *MB21D1* gene encoding cGAS (8.84-fold increase, FDR < 0.001)

and the *TMEM173* gene encoding STING (3.2-fold increase, FDR < 0.001), with associated enrichment for pathways related to cytosolic DNA sensing and innate immunity (Figures S5E and S5F). CDC also harbors multiple recurrent CNAs (Becker et al., 2013) and demonstrated similar levels of cGAS and STING gene expression (Supplementary Table 4). Furthermore, when compared with kidney MRT, a much more chromosomally stable disease (Figures 2E and S1E), RMC expressed significantly higher STING mRNA levels (4.2-fold increase, FDR < 0.001) and enrichment for cytosolic DNA sensing and innate immune pathways (Figures S5E and S5F). IHC confirmed the substantially higher presence of cytoplasmic STING in RMC compared with adjacent normal kidney and with kidney MRT tissues (Figures 5D and 5E).

DNA Replication Stress is a Hallmark of RMC

SMARCB1 in the SWI/SNF complex is known to antagonize c-MYC function by directly interacting with c-MYC target gene promoters (Stojanova et al., 2016; Weissmiller et al., 2019). Our GSEA analysis (Figure S3E) revealed that SMARCB1-deficient RMC tissues showed enrichment for multiple hallmark pathways associated with cell cycle progression and DNA replication and repair, including the G2-M checkpoint, c-MYC and E2F target genes, and TP53 and DNA repair pathways, consistent with these tumors having a replication stress phenotype (Zhang et al., 2016). Furthermore, RMC tumors exhibited an enrichment for expression of genes upregulated in response to activation of the ATR DNA damage repair pathway triggered by replication stress (Figure 6A). Kidney MRT tumors demonstrate a similar signature for MYC-induced replication stress and DNA damage repair (Figures S6A, S6B, and S6C). Furthermore, we found that gene sets associated with MYC-induced replication stress were upregulated in RMC (SMARCB1-negative) compared with CDC (SMARCB1-positive) tumors (Supplementary Table 4 and Figures 6B, 6C, and S6D). The c-MYC gene is located on chromosome 8q which we found to be gained in almost half of RMC tumors (Figures 2B and S2), with associated upregulation of *MYC* and other established regulators of the oncogenic MYC network such as *PVT1* (Tseng et al., 2014) and *ATAD2* (Ciro et al., 2009) (Supplementary Table 2).

In the mutational landscape of RMC we noted that the most common substitutions in most RMC tumors were C > T transitions (Figure 1), which are linked to the process of cytosine deamination often associated with age or DNA replication stress (Cescon and Haibe-Kains, 2016). However, patient age did not strongly correlate with the number of C > T mutations (Spearman rank correlation = 0.395, p = 0.145), suggesting that they are instead caused by replication stress in the setting of high cell turnover. Furthermore, the predominant mutational signature pattern in RMC tumors was Signature 1 (Figure S1C), which consists mainly of C > T transitions at CpG dinucleotide motifs and is known to be associated with age and/or high number of mitoses (Alexandrov et al., 2015). Again, however, there was no correlation between patient age and Signature 1 in our RMC samples (Spearman rank correlation = 0.167, p = 0.568). Thus, the genomic profile of RMC demonstrates mutational patterns compatible with replication stress.

SMARCB1 Loss Promotes MYC-induced Replication Stress

To perform *in vitro* functional experiments, we generated a new cell line (RMC2C) from the untreated primary tumor sample (RMC2T) of a male patient with RMC. The cell line grew in adherent monoculture (Figure S6E) with a doubling time of 32 hours for >40 passages. Spectral karyotyping (SKY) for this cell line revealed multiple CNAs as shown in Figure S6F. The near-tetraploid karyotype of RMC2C was not observed in the original RMC2T tumor (Figure S2). FISH demonstrated that both RMC2C and RMC2T harbored centromeric deletions of both *SMARCB1* alleles and no inactivating translocations (Supplementary Table 3). MLPA confirmed the absence of the *SMARCB1* gene in RMC2C cells (Figure S6G). We additionally used a previously established established RMC cell line (RMC219) (Dong et al., 2017), which is also negative for inactivating *SMARCB1* translocations and harbors centromeric deletions of both *SMARCB1* alleles (Supplementary Table 3 and Figure S6H). Karyotyping revealed loss of one copy of chromosome 22, gain of one copy of chromosome 8, as well as gain of two more 8q copies via two der(7)t(7q;8q) derivative chromosomes (Figure S6I). Supplementary Table 6 lists all RMC2C and RMC219 mutations detected by WES. From these cell lines, we also generated tet-inducible rescue lines capable of re-expressing SMARCB1 at near-endogenous levels (Figure S6J) and showed that exogenous SMARCB1 was incorporated into SWI/SNF complexes (Figure S7A).

As shown using our two RMC cell lines and two other SMARCB1-negative cell lines (MRT line G401 and epitheliod sarcoma line VA-ES-BJ) in Figure 6D, high c-MYC levels correlated with expression of the DNA damage marker γH2AX, expression of DNA damage repair enzymes Poly-(ADP-ribose) polymerase (PARP) and ataxia-telangiectasia and Rad3-related (ATR), ATR activation via phosphorylation at serine 428, upregulation and phosphorylation at serines 4 and 8 of the RPA32 subunit of human replication protein A (a marker of DNA damage response), upregulation of FANCD2 (which protects cells from replication stress), phosphorylation of CDK1 at tyrosine 15 (which regulates the G2-M checkpoint), as well as phosphorylation of TP53 at serine 15, a marker specific to DNA damage response and not to other stimuli such as hyper-proliferation (Loughery et al., 2014). Re-expression of SMARCB1 in all four lines decreased c-MYC activity and the resulting replication stress (Figure 6D). Similarly to rescue of SMARCB1, direct inhibition of c-MYC also reversed the replication stress cascade in these cells (Figure 6E). Conversely, *SMARCB1* knockout by CRISPR/Cas9 in human embryonic kidney (HEK-293FT) cells increased c-MYC and the resulting replication stress (Figures S7B and S7C). Figure S7D demonstrates the significant downregulation of γH2AX in the nuclei of RMC2C and RMC219 cells following rescue of SMARCB1.

We interrogated previously published chromatin immunoprecipitation sequencing (ChIP-Seq) data of c-MYC (Weissmiller et al., 2019) and found that tet-inducible re-expression of SMARCB1 in G401 MRT cells resulted in significant decrease (FDR < 0.05) of peaks at the promoter regions of genes associated with replication stress (Figures 6F and S7E). SMARCB1-negative G401 cells showed c-MYC enrichment at the promoter regions of genes associated with multiple hallmark pathways related to cell cycle progression and DNA replication and repair (Figure S7F). Similarly, we found that SMARCB1 re-expression in our RMC2C cells resulted in significant decrease of c-MYC enrichment at the promoters of

genes associated with cell cycle progression and DNA replication (Figure 6G). We performed DNA fiber assays to directly explore the effect of SMARCB1 loss on DNA replication fork dynamics. *SMARCB1* knockout significantly accelerated replication fork progression (Figure 6H), an established general mechanism of replication stress and associated DNA damage response (Maya-Mendoza et al., 2018). Collectively, our findings suggest that SMARCB1 loss increases c-MYC binding to the promoters of downstream genes associated with DNA replication and cell cycle progression, and induces replication stress by increasing the speed of replication fork progression with resultant upregulation of DDR pathways.

RMC is Vulnerable to Drugs Targeting Replication Stress I*n Vitro* and *In Vivo*

Tumors with high levels of replication stress depend on intact DDR pathways for survival (Zhang et al., 2016). We reasoned that as a result of this dependence, SMARCB1-negative tumors such as RMC would be vulnerable to direct targeting of DDR pathways such as the PARP and ATR pathways, or to targeting of cell cycle regulators such as the WEE1 kinase which suppresses replication stress (Beck et al., 2010). We first queried the Genomics of Drug Sensitivity in Cancer database (GDSC; release 7.0) (Yang et al., 2013) and found that the PARP inhibitor olaparib, clinically approved for use in breast and ovarian cancer, induces a more potent antiproliferative response in the SMARCB1-negative MRT cell line G401 than that seen in *BRCA1*-mutant cell lines such as HCC1395 and HCC1937 or most other breast and ovarian cancer cell lines (Supplementary Table 7). Subsequently, we confirmed *in vitro* using two separate PARP inhibitors (olaparib and niraparib) that, compared with three SMARCB1-positive renal cell carcinoma cell lines, SMARCB1-negative cell lines are sensitive to targeting of the PARP pathway (Figure 7A). We also found that SMARCB1-negative cell lines are sensitive to the ATR inhibitors VX970 and AZD6738 and to the WEE1 inhibitor adavosertib (Figure 7B). Rescuing of SMARCB1 or directly inhibiting c-MYC reversed the sensitivity of SMARCB1-negative cells to PARP, ATR, and WEE1 inhibitors (Figures 7C and 7D). Collectively, these data demonstrate that SMARCB1 loss sensitizes cancer cells to pharmacologic perturbation of the DDR and cell cyle checkpoint pathways. Sensitivity to platinum salts such as cisplatin and carboplatin, DNA synthesis inhibitors such as gemcitabine, and topoisomerase inhibitors such as doxorubicin is a hallmark of tumors with high levels of replication stress because these drugs can induce or augment DNA damage, which can overwhelm DDR pathways thus leading to insurmountable genomic instability and cell death (Zhang et al., 2016). We accordingly found that the sensitivity of RMC cell lines to these agents is significantly reduced by either rescuing of SMARCB1 or direct inhibition of c-MYC (Figures S7G and S7H).

To investigate the *in vivo* antitumor effect of targeting DDR pathways in RMC, we used a subcutaneous patient-derived xenograft (PDX) model (RMC2X) generated from the untreated primary tumor sample (RMC2T) of a male patient with RMC. Mice harboring RMC2X tumors (n = 5 per group; average tumor volume of 158 mm^3 at treatment initiation) were randomly assigned to receive niraparib, AZD6738, the combination of niraparib with AZD6738, or vehicle control for a total of 25 days. One mouse in the control group died on day 8 after treatment initiation, whereas all mice in the three treatment groups were alive by

the end of treatment. As shown in Figure 7E, treatment with niraparib led to significantly lower tumor volume compared with vehicle control ($p = 0.0196$). Conversely, treatment with AZD6738 did not significantly reduce tumor volume compared with vehicle control ($p = 0.54$), and its combination with niraparib did not produce a stronger antitumor effect compared with niraparib alone ($p = 0.868$). The treatments were well-tolerated, with no significant reduction in animal body weight compared with vehicle control (Figure S7I). The addition of niraparib to cisplatin produced higher antitumor efficacy than either agent alone (Figure 7F). These findings suggest the potential therapeutic value of targeting the PARP pathway alone or in combination with platinum chemotherapy in RMC.

DISCUSSION

In contrast to the low number of focal CNAs found in MRT and ATRT (Chun et al., 2016; Hasselblatt et al., 2013; Takita et al., 2014), we found that RMC harbors a much more complex genome with high levels of focal CNAs with approximately one-third mapped to chromosomal fragile sites. This is consistent with our previously hypothesized model of RMC pathogenesis whereby red blood cell sickling in individuals with sickle cell trait induces chromosomal structural alterations in renal medullary cells, particularly in hotspots for chromosomal rearrangements (Msaouel et al., 2018). We found that one copy of chromosome 22, which harbors SMARCB1, is lost in over a third of RMC tumors. The only other recurrent arm-level CNA, observed in approximately half of RMC tissues, was 8q gain where the *c-MYC* gene is located. In addition, we found that RMC tumors contain recurrent focal CNAs in regions of genes related to cell proliferation, including a distinct CNA pattern that results in Notch pathway activation and is also found in the basal subtype of BLCA (Hayashi et al., 2016).

We found that a notable distinction between RMC and CDC is that SMARCB1 loss in RMC activates the c-MYC pathway and subsequently induces high levels of DNA replication stress resulting in the upregulation of DDR and cell cycle checkpoint pathways compared with CDC. CNAs in chromosomal fragile sites such as those noted in RMC can be both a source and a consequence of DNA replication stress in cancer cells (Zeman and Cimprich, 2014). Therefore, the abundance of chromosomal alterations in RMC may confer a higher sensitivity to therapies that harness replication stress compared with SMARCB1-negative malignancies with more simple genomes such as MRT and ATRT. Platinum-based chemotherapy is currently the recommended standard of care therapy for RMC (Msaouel et al., 2019). Furthermore, the combination of gemcitabine with doxorubicin, targeting replication stress, is one of the most clinically active cytotoxic chemotherapy regimens used for the treatment of RMC (Shah et al., 2017). Aberrant c-MYC activity in the setting of SMARCB1 loss also upregulates the unfolded protein response (UPR), thus making cells susceptible to agents that induce proteotoxic stress such as ixazomib (Carugo et al., 2019; Genovese et al., 2017). We have accordingly activated an ongoing clinical trial (NCT03587662 at clinicaltrials.gov) testing the efficacy of ixazomib in combination with gemcitabine and doxorubicin in patients with RMC. We further identified and demonstrated both *in vitro* and *in vivo* that RMC is vulnerable to direct targeting of DDR pathways. Of note, the combination of niraparib to platinum produced significantly better *in vivo* antitumor responses. PARP inhibitors such as olaparib, niraparib, and rucaparib have now

been clinically approved for the treatment of multiple malignancies as single-agent therapies or in sequence with cytotoxic chemotherapy (Cook and Tinker, 2019). The extensive clinical experience with these agents and the efficacy shown in our preclinical models makes clinical testing of PARP inhibitors in patients with RMC a logical next step.

SMARCB1 loss was recently shown to induce interferon-mediated immunogenicity in rhabdoid tumors (Leruste et al., 2019). The highly inflamed phenotype of RMC in the setting of low tumor mutational burden and high number of focal CNAs and replication stress led us to identify the cGAS-STING pathway as a distinct source of pro-inflammatory signaling in this malignancy. We have activated an ongoing biopsy-driven clinical trial (NCT03274258 at clinicaltrials.gov) to better delineate how the distinct immune profile of RMC affects the efficacy of currently approved immune checkpoint therapies. Figure 7G depicts our schematic model of the inflammatory responses and replication stress induced by the crosstalk between SMARCB1 loss and CNAs in RMC. It should be noted that our genomic sequencing lacked the sensitivity to detect rare subclonal alterations and further studies will be needed to delineate the intratumoral mutational and copy number heterogeneity of RMC.

In summary, our study has revealed several insights into the molecular foundations of RMC. We found that RMC is defined by a high number of focal CNAs and harbors a distinct immune microenvironment compared with other renal cell carcinomas paving the way for future studies assessing the role of the cGAS-STING pathway in the immunotherapy of RMC. Furthermore, we identified the importance of SMARCB1 loss as a major recurrent genetic alteration in RMC and found that it confers replication stress-induced vulnerabilities that can be therapeutically targeted. These results highlight a potential opportunity to utilize agents targeting replication stress pathways alone or in combination with other therapies to yield deep and durable therapeutic responses.

STAR METHODS

Lead Contact and Materials Availability

Further information and requests for resources and reagents should be directed to and will be fulfilled by the Lead Contact, Pavlos Msaouel (pmsaouel@mdanderson.org).

Experimental Models and Subject Details

Tumor samples—Tumor samples were obtained from 38 patients with RMC, 9 patients with CDC, and 22 patients with UTUC using endoscopic biopsy or surgical resection. Histology slides were reviewed by a genitourinary pathology expert (Priya Rao) and the RMC samples were all confirmed to be SMARCB1 negative by immunohistochemistry using purified mouse anti-BAF47 Clone 25/BAF47 (BD Biosciences) as shown in Figure S1A. CDC samples were all SMARCB1 positive by the same immunohistochemical assay and were derived from untreated primary tumors. Sickle cell status was determined by hemoglobin electrophoresis. Figure 1 lists patient characteristics and also provides RMC sample annotation, clinical details, and the assays performed on each sample. This study was

performed under Institutional Review Board-approved protocols (PA11–1045 and PA19–0250) and conducted in accordance with the principles of the Declaration of Helsinki.

Generation and authentication of new RMC cell line—The new RMC cell line RMC2C was derived from the untreated primary nephrectomy specimen (corresponding to the RMC2T tumor sample) of a 35-year-old African American male patient with sickle cell trait using previously reported methodology (Karam et al., 2011). Cell line authentication was performed by short tandem repeat (STR) DNA profiling (Kerrigan and Nims, 2011) in direct comparison with the primary patient-derived tissue. RMC2C was cultured at 37°C in minimum essential medium (MEM) supplemented with MEM non-essential amino acids, EGF (5 μg/mL), 100 U/mL penicillin-streptomycin, and 10% heat-inactivated fetal bovine serum. Cell line doubling time was calculated as: duration of culture * ln(2) / ln(final cell number - initial cell number).

Commercial and other cell lines—G401, CHLA-06-ATRT, VA-ES-BJ, A-498, and 786-O were purchased from American Type Culture Collection (ATCC, Manassas, VA). HEK-293FT were purchased from Thermo Fisher Scientific (Waltham, MA). All cell lines were grown at 37 °C in media recommended by ATCC in a humidified atmosphere of 5% CO_2. The RCC4 cell line was purchased from the European Collection of Authenticated Cell Cultures (ECACC, Porton Down, Salisbury, United Kingdom) and was grown at 37 °C in the medium recommended by ECACC in a humidified atmosphere of 5% CO_2. The RMC219 cell line (also designated as JHRCC219) was established from a previously described patient-derived xenograft (Dong et al., 2017) derived from the bone metastasis of a 39 year old African American male patient with sickle cell trait who was previously treated with 5 cycles of gemcitabine and carboplatin for metastatic RMC. RMC219 was cultured at 37°C in Ham's F-12 medium supplemented with 1% essential amino acids, 1% sodium pyruvate, and 1% L-glutamine. All media contained 100 U/mL penicillin-streptomycin and were supplemented with 10% heat-inactivated fetal bovine serum. We monitored all cell lines for mycoplasma every 3 months using the Universal Mycoplasma Detection Kit by ATCC (Manassas, VA). All cell lines were refreshed from frozen early-passage stock after approximately 20 passages.

Generation of RMC PDX model—The new RMC2X PDX model was derived from the untreated primary nephrectomy specimen (corresponding to the RMC2T tumor sample) of a 35-year-old African American male patient with sickle cell trait. The banked RMC2X tumor was implanted into the subcutaneous tissue of immunodeficient female CB17/lcr-Prkd^{scid}/lcrlcoCrl mice aged 6–9 weeks old using previously reported methodology (Kim et al., 2009). PDX authentication was performed by short tandem repeat (STR) DNA profiling (Kerrigan and Nims, 2011) in direct comparison with the primary patient-derived tissue.

Mouse Studies

Female CB17/lcr-Prkd^{scid}/lcrlcoCrl mice were obtained by Charles River. Mice aged 6–9 weeks old were used for all PDX transplantation studies. All animal studies and procedures were approved by the UTMDACC Institutional Animal Care and Use Committee (protocols

00001200 and 00000884). All experiments conformed to the relevant regulatory standards and overseen by the institutional review board.

Method Details

WES and targeted DNA sequencing—Genomic DNA was isolated from formalin-fixed paraffin-embedded (FFPE) samples using QIAamp DNA FFPE Tissue kit (Qiagen) and from fresh frozen tissue using the AllPrep DNA/RNA Mini Kit (Qiagen). Figure 1 lists the patient samples where fresh frozen tissue (tumor tumor and, where available, adjacent normal kidney) was available for WES. Illumina-compatible exome libraries were prepared from 200 ng of Bioruter Ultrasonicator (Diagenode) sheared RNase treated gDNA using the Agilent SureSelectXT Reagent Kit (Agilent Technologies). Libraries were uniquely indexed and prepared for capture with 8 to 11 cycles of PCR amplification, then assessed for size distribution on 4200 TapeStation High Sensitivity D1000 ScreenTape (Agilent Technologies) and quantified using the Qubit dsDNA HS Assay Kit (ThermoFisher Scientific). Exon target capture was performed using the Agilent SureSelectXT Human All Exon V7 Target Enrichment Baits. Following capture, the exon-enriched libraries were amplified using nine cycles of PCR, then assessed for size distribution using the Agilent TapesStation and quantified using the Qubit dsDNA HS Assay Kit. Libraries were multiplexed with eight samples per pool and the pools were quantified by qPCR using the KAPA Library Quantification Kit (Roche). The pool was sequenced in one lane of the HiSeq 4000 sequencer using the paired-end format.

To minimize sequence artifacts from FFPE-derived DNA, all tissue samples were less than one year old and were first reviewed by a genitourinary pathology expert (Priya Rao) to identify tumor-rich areas (or adjacent normal kidney where applicable) prior to proceeding with DNA isolation. We removed formaldehyde-induced crosslinks using a heat treatment step prior to sequencing as described in the QIAamp DNA FFPE Tissue kit (Qiagen). We followed rigorous quality control methods and used a high-fidelity capture-based sequencing approach using the Agilent SureSelectXT Human All Exon V7 Target Enrichment Baits known to perform well with FFPE samples (Do and Dobrovic, 2015). Baseline noise during sequencing of FFPE samples is in large part due to cytosine deamination. This usually occurs in one strand and not both DNA strands (Do and Dobrovic, 2015). Thus, we required that each specific mutant allele had to be detected in both strands in order to be called positive. This restriction allowed us to reliably distinguish true mutations from sequence artifacts.

The average mean target WES coverage was 73-fold for RMC tumor tissues and 60-fold for matched normal tissue, with a mean estimated tumor purity of 49.1% (range, 24%–98%). Previous benchmarking (Cibulskis et al., 2013) has demonstrated that our approximately 70-fold mean WES depth provided a >97% sensitivity to detect somatic mutations present in as low as 20% of sequenced cells, representing an expected mutation allele fraction of 0.1 (assuming that heterozygous mutations are present in a diploid region). However, more rare somatic mutations such as those present in 8% of sequenced cells would be detected with a sensitivity of approximately 53%. Thus, although our WES had high sensitivity to detect

dominant clonal or subclonal RMC tumor mutations, it would be less likely to detect more rare subclonal alterations.

Confirmatory Sanger sequencing was performed at the MD Anderson Cancer Center Sequencing and Microarray Facility using Big Dye terminator cycle sequencing chemistry. We additionally performed hybrid capture-based targeted DNA sequencing in FFPE samples using FoundationOne CDx (Frampton et al., 2013) for untreated primary tumor samples from patients RMC5, RMC18, RMC20, and RMC27, as well as PCR-amplicon-based target capture using Oncomine (Luthra et al., 2017) for samples RMC4, RMC16, and RMC22. Gene Ontology analysis was carried out using DAVID release 6.8 with default parameters for biological processes (GOTERM_BP_FAT) (Huang da et al., 2009a; Huang da et al., 2009b).

Somatic mutation detection from whole exome sequencing—The raw paired-end (PE) reads in FASTQ format were aligned to the human reference genome (hg19), using the MOSAIK alignment software (Lee et al., 2014). We then analyzed the resulting alignments with PCR duplicate removal using the Bayesian model-based software GigaBayes/FreeBayes (Marth et al., 1999), which enables efficient analysis of billions of aligned short-read sequences. The program evaluates each aligned base and its base quality value at each position to indicate putative single-nucleotide variations (SNVs) and short insertions/deletions (inDels), and their corresponding SNV probability value (P_{SNV}). Base quality values are converted to base probabilities corresponding to every one of the four possible nucleotides. Using a Bayesian formulation, a P_{SNV} (or inDel probability value, as appropriate) is calculated as the likelihood that multiple different alleles are present between the reference genome sequence and the reads aligned at that position. If the probability value exceeds a pre-specified threshold, the SNV or inDel candidate is reported in the output. We used a P_{SNV} cutoff value of 0.9 to define a high-confidence SNV or short inDel candidate. We also filtered out all known SNVs/inDels in UCSC dbSNP 142 (human). Furthermore, we required that a specific mutant allele had to be detected at least 6 times, and in both strands at least once, in order to be considered an SNV or inDel candidate. We then determined the somatic status of each SNV (or inDel) by comparing the genotypes and their likelihood in matched tumor and germline samples when available. The somatic status of a specific SNV/inDel was reported once the matched germline had wild allele-based homozygous genotype and the tumor had heterozygous or mutant allele-based homozygous genotype with a certain cutoff of genotype likelihood/p value of 0.99. Each somatic mutation or inDel was annotated with functional effect by SIFT (Vaser et al., 2016) to determine if a mutation candidate was synonymous or non-synonymous.

To maximize specificity in mutational signature analysis, we only used the 15 RMC samples with available germline tissue to calculate mutational signature weights. Sample RMC36T1 was excluded from further analysis because it lacked SNVs. All SNVs in a sample can be allocated to one of 96 “bins” according to the “before/after” status of the initial pyrimidine and the nucleotides on either side. The final vector of 96 bin counts defines a “mutational context histogram” (MCH) characterizing that sample. Particularly common MCH patterns can be used to define mutational “signatures” which may be indicative of modes of mutagenesis. The Sanger institute maintains a canonical set of 30 mutational signatures

(http://cancer.sanger.ac.uk/cosmic/signatures) identified by applying non-negative matrix factorization (NMF) to the MCHs of thousands of tumors (Alexandrov et al., 2013). Taking these signatures as given, we can "score" the MCH of a new sample for the relative contributions of each signature using quadratic programming. We obtained the neighboring bases of each SNV using the R package, BSgenome.Hsapiens.UCSC.hg19 (version:1.4.0) (The Bioconductor Dev Team, 2014).

Comparison of non-synonymous mutation load per genome for different tumor types (shown in Figure 2A) was performed using our sequencing data from RMC as well as previously published DNA sequencing data (Chun et al., 2016) from 34 patients with MRT originating from the kidney, as well as tumors sequenced by The Cancer Genome Atlas (TCGA; http://cancergenome.nih.gov/). Tumors were abbreviated as per the following: ACC, adrenocortical carcinoma; BLCA, bladder urothelial carcinoma; BRCA, breast invasive carcinoma; ccRCC, clear cell renal cell carcinoma; CESC, cervical squamous cell carcinoma & endocervical adenocarcinoma; ChRCC, chromophobe renal cell carcinoma; COAD, colon adenocarcinoma; GBM, glioblastoma; HNSC, head & neck squamous cell carcinoma; LAML, acute myeloid leukemia; LGG, low grade glioma; LIHC, hepatocellular carcinoma; LUAD, lung adenocarcinoma; LUSC, lung squamous cell carcinoma; MRT, malignant rhabdoid tumor of the kidney; OV, ovarian serous cystadenocarcinoma; PAAD, pancreatic adenocarcinoma; PCPG, pheochromocytoma & paraganglioma; PRAD, prostate adenocarcinoma; PRCC, papillary renal cell carcinoma; READ, rectal adenocarcinoma; RMC, renal medullary carcinoma; SKCM, skin cutaneous melanoma; STAD, stomach adenocarcinoma; THCA, papillary thyroid carcinoma; UCEC, uterine corpus endometrial carcinoma; UCS, uterine carcinosarcoma.

Identification of copy number alterations—Copy number analyses were performed on WES data of the 15 RMC samples with available germline tissue to improve the specificity of our results. The aligned reads were processed by our inhouse R package, ExomeCN (Zhang et al., 2014), followed by Circular Binary Segmentation (Olshen et al., 2004). ExomeCN is a modified version of HMMcopy (Ha et al., 2012) tuned for our data. Sequenza (Favero et al., 2015) with default parameters was used to estimate cellularity and ploidy and to identify and visualize copy number alterations (CNAs) per sample. Recurrent focal somatic CNAs were detected and localized using GISTIC2.0 (Mermel et al., 2011) (Beroukhim et al., 2010) with the thresholds of copy number amplifications/deletions being equal to ± 0.15 and q-value threshold being equal to 0.2. For comparison, we performed GISTIC2 analyses using the same parameters in previously published WES results from 35 patients with MRT and ATRT (Lee et al., 2012), comprised of 22 cases of ATRT, 4 cases of kidney MRT, and 9 cases of MRT arising from other soft tissues. Arm-level copy number alterations are defined by GISTIC as those exceeding half the length of a chromosome arm, whereas focal copy number alterations are those shorter than half the length of a chromosome arm. Using cytoband data from hg19 (http://hgdownload.cse.ucsc.edu/goldenpath/hg19/database), we defined 8q gain as a gain in the following genome coordinates of chromosome 8: 45,600,000 to 146,364,022. Using these coordinates, a total of 376 protein-coding genes and 334 lncRNA genes from our RNA-seq profiling were mapped to the chromosome 8q arm.

Validation of WES copy number findings was performed using high-resolution oligonucleotide comparative genomic hybridization (CGH) arrays using standard operating procedures from Agilent Technologies (Agilent Oligonucleotide Array-Based CGH for Genomic DNA Analysis G4410–90010). Double enzymatic digestion (Alu I + Rsa I) was used to fragment 500 ng of DNA which was then evaluated with LabOnChip (2100 Bioanalyzer System; Agilent Technologies) prior to labeling and hybridization. Control DNA was used from Promega (Human Genomic DNA Female N 30742202/Male N 30993901). DNA was labeled by random priming with CY5-dCTPs (tumor DNA) and CY3-dCTPs (control DNA), and was hybridized to 4×180K whole-genome Agilent arrays (G4448A). Agilent G2565BA DNA Microarray Scanner was used to scan the chips. Image analysis and fluorescent signal acquisition were performed using the Feature-Extraction V9.1.3 software (Agilent Technologies).

RNA sequencing—RNA was extracted from fresh frozen RMC (n = 11 cases), CDC (n = 9 cases), UTUC (n = 22 cases), and adjacent normal kidney (n = 6 patients with RMC) tissue samples using the RNeasy Kit (Qiagen) according to the manufacturer's instructions. Normal kidney tissues were obtained from locations at least 2 cm away from the primary tumors and the absence of metastatic cells was confirmed by a genitourinary pathology expert (Priya Rao). As a comparator, we used previously published RNA sequencing data (Chun et al., 2016) from 56 patients with MRT originating from the kidney (Supplementary Table 4). As an additional control we randomly selected a dataset from The Cancer Genome Atlas (TCGA), comprised of ccRCC (n = 20 cases) (Cancer Genome Atlas Research, 2013), PRCC (n = 20 cases) (Cancer Genome Atlas Research et al., 2016), and ChRCC (n = 20 cases) (Davis et al., 2014) listed in Supplementary Table 4.

After controlling for the quality of the initial samples, rRNA depletion was performed for the total RNA for each sample, followed by random-primed and stranded cDNA preparation and quality control. Total RNA was converted into a library of template molecules for sequencing on Illumina HiSeq2000, with a paired-end read length of 100 to 125 nt. The quality of the FASTQ reads was evaluated using the FastQC software (Andrews, 2014). The raw reads in FASTQ format were aligned to the reference human genome, hg19, using the MOSAIK alignment software (Lee et al., 2014). Gap alignment was performed using the Smith-Waterman algorithm in MOSAIK. Gene-level annotation was carried out using the GENCODE annotation, which was downloaded from the GENCODE project (Harrow et al., 2012). The overlaps between aligned reads and annotated genes were counted using HTSeq software (Anders et al., 2015). Gene counts were normalized using the scaling factor method. If the number of overlapped reads of any given gene was less than one per million total mapped reads for all samples, this gene was excluded from further analysis. Hierarchical clustering analyses were performed using the Pearson correlation coefficient as the distance metric and the ward's linkage rule. Principle component analyses (PCA) were also performed to explore the multi-gene structure. A negative binomial model was fit to the read counts of each gene. Then a Wald test was used to test the null hypothesis of no difference in gene expression between two conditions, e.g., tumor vs normal samples. The Benjamini & Hochberg (BH) method was used to control false discovery rate (FDR). These

methods were implemented in the DESeq2 (Love et al., 2014) run on R version 3.2.3. Pathway diagram templates were taken from Chen et al. (Chen et al., 2018).

Virus integration analyses—The VirusSeq algorithmic method (http://odin.mdacc.tmc.edu/~xsu1/VirusSeq.html) was used to identify, as previously described (Chen et al., 2013), the following viruses and their integration sites from RNA-seq data: BK polyomavirus, cytomegalovirus, Epstein-Barr virus, hepatitis B virus, hepatitis C virus, human herpesvirus 1, human T-lymphotropic virus, human polyomavirus 2 (JC virus), Kaposi's sarcoma-associated herpesvirus, as well as human papillomavirus strains 6, 16, 18, 26, 30, 31, 33, 34, 35, 45, 52, 56, 58, 59, 68, 69, and 70.

Analysis of kidney nephron atlas expression data—We used the gene expression profiles from different nephron sites (both human and mouse) obtained from the study by Cheval et al (Cheval et al., 2012). For each gene in our kidney cancer dataset (combined RMC, CDC, ccRCC, PRCC, ChRCC, and kidney MRT) we centered expression values on the mean centroid of these malignancies. Within each of the human and mouse datasets from the Cheval et al study, we centered values on the median across samples. Using the centered datasets for each kidney malignancy and the Cheval et al mRNA profile, we computed the global inter-profile correlation (by Pearson's), using all ~4000 genes in common, as previously described (Davis et al., 2014).

Gene set enrichment analysis (GSEA)—We performed GSEA (Subramanian et al., 2005) of RNA-seq data using the R-GSEA script run in R version 3.2.3 using the following gene sets collected at the Molecular Signatures Database (MSigDB) (http://software.broadinstitute.org/gsea/msigdb/collections.jsp): (i) Fifty hallmark gene sets, which summarize and represent specific well-defined biological states or processes and display coherent expression. These gene sets were generated by a computational methodology based on identifying overlaps between gene sets in other MSigDB collections and retaining genes that display coordinate expression (Liberzon et al., 2015); (ii) Canonical pathway gene sets curated from online databases including BIOCARTA, KEGG, and REACTOME; (iii) Gene Ontology (GO) gene sets.

Deconvolution of tissue-infiltrating immune and stromal cell populations—We used the Microenvironment Cell Populations-counter (MCP-counter) method (MCPcounter 1.1.0 package run on R version 3.2.3) to deconvolute and quantify eight immune and two stromal cell populations from RNA-seq data. The resulting scores for each cell type were then Z-transformed. For each sample, MCP-counter produces an abundance score for $CD3^+$ T cells, $CD8^+$ T cells, cytotoxic lymphocytes, NK cells, B lymphocytes, monocytic lineage cells, myeloid dendritic cells, neutrophils, endothelial cells, and fibroblasts. Because MCP-counter scores are independently computed for each individual sample, they can be used for direct comparisons of cell type abudance across different samples (Becht et al., 2016).

DNA methylation analysis—DNA methylation was assessed using the Illumina Infinium HumanMethylation450 (HM450) BeadChip array in three untreated primary RMC tumor samples (PED4T, MED3T, and RMC8T), as well as normal kidney control samples from four patients with RMC (RMC2N, RMC4N, RMC5N, and RMC8N). Bisulfite convertion of

genomic DNA (500–1000 ng) was performed using the Zymo EZ DNA methylation kit (Zymo Research, Irvine, CA) according to the manufacturer's recommendations. The quantity of bisulfite-converted DNA and the completeness of bisuflite conversion for each sample were assessed using a panel of MethyLight-based real-time PCR quality control assays as previously described (Campan et al., 2009). Bisulfite-converted DNA was subsequently used as a substrate for the HM450 BeadArrays, as recommended by the manufacturer. Specifically, each sample was whole-genome amplified (WGA), enzymatically fragmented, and then hybridized overnight to an 8-sample BeadArray, in which the WGA-DNA molecules annealed to locus-specific DNA oligomers linked to individual bead types. After the chemical processes, BeadArrays were scanned and the 'noob' function in the minfi R package (Aryee et al., 2014), which corrects for background fluorescence intensities and red-green dye bias (Triche et al., 2013), was used to extract raw signal intensities from the *.IDAT files. Probe alignment was performed using the hg19/GRCh37 human genome assembly. The beta (β) value for each probe was calculated using the formula $\beta = M/(M+U)$, in which M and U respectively refer to the (pre-processed) mean methylated and unmethylated probe signal intensities. The average β value reports a methylation signal ranging from 0 to 1, respectively representing completely unmethylated to completely methylated values. Probes in promoter CpG islands of *SMARCB1* with β-value ≤ 0.2 were considered unmethylated and those with β-value ≥ 0.3 were considered methylated.

Fluorescence in situ hybridization (FISH)—FISH was performed on paraffin sections according to the manufacturer's protocol using SMARCB1BA-20-GROR Break Apart probe (Empire Genomics) which is telomeric (orange label) and centromeric (green label) to the *SMARCB1* gene. Signal counts were performed on captured images of at least 50 non-overlapping tumor nuclei in two separate areas of a population of tumor cells. Samples with break-apart in ≥ 15% of tumor nuclei were considered positive for *SMARCB1* translocation. Partial *SMARCB1* deletion was defined as loss of either green or orange probes in ≥ 15% of tumor nuclei. Whole *SMARCB1* allele deletion was defined as ≥ 60% loss of both green and orange probes.

Multiplex ligation-dependent probe amplification (MLPA)—MLPA was performed on genomic DNA according to the manufacturer's protocol using the SALSA MLPA P258 (*SMARCB1*) kit (MRC-Holland). This kit includes 2 probes for each of the 9 exons of *SMARCB1*, as well as probes for 9 other genes on chromosome 22 (*TBX1* exons 2 and 7, *DGCR8* exon 2, *SNAP29* exon 3, *LZTR1* exon 16, *PPIL2* exon 20, *GNAZ* exon 2, *SNRPD3* exon 2, *SEZ6L* exon 2, and *NIPSNAP1* exon 10), as well as 14 control probes for genes located on other chromosomes: *TNNT2* (chromosome 1), *POMC* (chromosome 2), *EDAR* (chromosome 2), *BMPR2* (chromosome 2), *CASR* (chromosome 3), *IL4* (chromosome 5), *PKHD*1 (chromosome 6), *PCDH15* (chromosome 10), *BEST1* (chromosome 11), *CSK* (chromosome 15), *FANCA* (chromosome 16), *CACNA1A* (chromosome 19), *JAG1* (chromosome 20), and *KCNJ6* (chromosome 21). Samples were processed and data were analyzed as previously described (Jalali et al., 2008). Dosage quotient (DQ) ratios were calculated and interpreted as follows: DQ = 0: homozygous deletion; 0.4 ≤ DQ ≤ 0.65: heterozygous deletion; 0.7 < DQ < 1.3: normal (identical to reference samples); 1.3 < DQ <

1.65: heterozygous duplication; 1.75 < DQ < 2.15: duplication; all other values: ambiguous result. All MLPA assays were performed in duplicate.

Spectral karyotyping and G-banding—Exponentially growing cells were exposed to Colcemid (0.04 μg/mL) for one hour at 37 °C and to hypotonic treatment (0.075 M KCl) for 20 minutes at room temperature. Cells were fixed in a methanol and acetic acid (3:1 by volume) mixture for 15 min and washed three times in the fixative. Slides were prepared by dropping the cell suspension on wet slides and air drying.

G-banding was performed using trypsin solution and stained in Giemsa. Spectral karyotyping (SKY) was conducted according to the manufacturer's protocol using the human chromosome HiSKY probe (Applied Spectral Imaging, Inc.). A minimum of 18 metaphases were analyzed. Images were captured using a Nikon 80i microscope equipped with the HiBand spectral karyotyping software from Applied Spectral Imaging, Inc (Vista, CA).

SMARCB1 re-expression experiments—We used the tetracycline-inducible pIND20-fSNF5-HA vector (Wei et al., 2014) kindly donated by Dr. Bernard E. Weissman. The pInducer20 empty backbone (Meerbrey et al., 2011) was a gift from Stephen Elledge (Addgene plasmid # 44012 ; http://n2t.net/addgene:44012 ; RRID:Addgene_44012). Lentivirus was generated in HEK-293FT cells and used to generate stable tet-inducible cell lines as previously described (Xu et al., 2001). All plasmid vectors were propagated in the E. coli strain DH5α (Invitrogen; Cat#18265017). For all SMARCB1 re-expression experiments, unless otherwise specified, a doxycycline concentration of 0.5 μg/mL was used for 3 days in cells harboring the tetracycline-inducible pIND20-fSNF5-HA vector or the pInducer20 empty backbone control.

Western blot analyses—Protein concentrations were measured by Pierce BCA protein assay kit. Before loading, samples were mixed with an equal volume of Laemmli Sample Buffer (Bio-Rad), heat denatured (100°C, 10 min) with β-mercaptoethanol (β-ME; Sigma-Aldrich), loaded in precast SDS/PAGE gels (Bio-Rad), transferred to PVDF membranes, and probed with specific primary antibodies overnight at 4°C. The following day, they were probed with secondary anti-mouse or anti-rabbit IgG conjugated horseradish peroxidase antibody, and chemiluminescence was detected by film exposure. The following primary antibodies were used: mouse monoclonal anti-SMARCB1 antibody clone 2C2 (Sigma-Aldrich; SAB4200202), rabbit polyclonal anti-phospho-Histone H2A.X at serine 139 (γH2AX; Cell Signaling Technology; 2577), mouse monoclonal anti-c-MYC antibody 9E10 (Santa Cruz Biotechology; sc-40), rabbit polyclonal anti-PARP (Cell Signaling Technology; 9542), goat polyclonal anti-ATR (Santa Cruz Biotechnology; sc-1887), rabbit polyclonal anti-phospho-ATR at serine 428 (Cell Signaling Technology; 2853), mouse monoclonal anti-TP53 (Santa Cruz Biotechnology; sc-126), rabbit polyclonal anti-phospho-TP53 at serine 15 (Cell Signaling Technology; 9284), mouse monoclonal anti-actin (Santa Cruz Biotechnology; sc- 47778), rabbit polyclonal anti-phospho-CDK1 at tyrosine 15 (Cell Signaling Technology; 9111), mouse monoclonal anti-RPA 32 kDa subunit 9H8 (Santa Cruz Biotechology; sc-56770), rabbit polyclonal anti-phospho-RPA32 at serines 4 and 8 (Bethyl

Laboratories; A300–245A), mouse monoclonal anti-FANCD2 (Santa Cruz Biotechology; sc-20022).

To reduce non-specific signals, membranes were blocked in 3% bovine serum albumin (BSA) or Odyssey blocking buffer (Licor). Membranes were incubated with indicated primary antibodies overnight at 4°C, washed in TBST buffer, and probed with HRP-conjugated secondary antibodies at room temperature for one hour. The detection of bands was carried out upon chemiluminescence reaction followed by film exposure. Western blots in the SMARCB1 rescue experiments were obtained after 5 days of doxycycline treatment. Western blots in the c-MYC knockdown experiments were obtained 3 days after MYC siRNA inhibition.

Co-immunoprecipitation experiments—SMARCB1 was immunoprecipitated from cell extracts using anti-SMARCB1 antibody (Sigma-Aldrich; SAB4200202) and protein A/G agarose beads (Santa Cruz Biotechnology) using 1X cell lysis buffer [20 mM Tris-HCl (pH 7.5), 150 mM NaCl, 1 mM EDTA, 1 mM EGTA, 1% Triton X-100, and protease inhibitor cocktail (Roche)]. The immunoprecipitated complex was washed using phosphate-buffered saline (PBS) (3.2 mM Na_2HPO_4, 0.5 mM KH_2PO_4, 1.3 mM KCl, 135 mM NaCl, pH 7.4) containing 1% Triton X-100 (PBST). Following immunoprecipitation, the samples were subjected to SDS-PAGE gel electrophoresis under denaturing conditions, and subsequently immunoblotted using antibodies against PBRM1 (rabbit polyclonal; Bethyl Laboratories, A301–591A), SMARCA4 (rabbit monoclonal; Abcam; ab110641), and ARID1A (mouse monoclonal; Santa Cruz Biotechnology; sc-32761). TrueBlot anti-rabbit or mouse IgG-HRP (Rockland) were used as secondary antibodies.

Immunohistochemistry—Immunohistochemistry (IHC) was performed on FFPE tumor tissue sections. The tumor tissues were fixed in 10% formalin, embedded in paraffin, and transversely sectioned. Four-μm sections were used for the IHC analyses. The sections were stained with a rabbit anti-human monoclonal antibody against STING (Cell Signaling, clone D2P2F; 13647S, dilution 1:100), PD-L1 (Cell Signaling, 13684S; 1:100), and PD-1 (Abcam, AB201825; 1:250), rabbit anti-human polyclonal antibody against CD3 (Agilent, A0452, 1:100), and mouse anti-human monoclonal antibodies against CD4 (Leica Biosystems, NCL-L-CD4–368; 1:80), CD8 (Thermo Scientific, MS-457-S; 1:25), FOXP3 (BioLegend, clone 206D, dilution 1:50), CD20 (Agilent; L26, 1:1,400), and CD68 (Agilent, M0876; 1:450). All slides were stained as previously described (Chen et al., 2016) using previously optimized conditions with appropriate positive and negative controls. The IHC reaction was detected using the Leica Bond Polymer Refine detection kit (Leica Biosystems) with diaminobenzidine (DAB) used as chromogen. Counterstaining was done using hematoxylin. IHC and hematoxylin- and eosin-stained slides were converted into high-resolution digital images using an Aperio slide scanner (Aperio AT Turbo, Leica Biosystems). Quantitative IHC staining of CD3, CD4, CD8, CD20, CD68, FOXP3, PD-1, and PD-L1 was evaluated by quantification of the density of positive cells (defined as the number of positive cells per mm^2), percentage of positive cells, and H-score as previously described (Parra et al., 2016). Quantitative analysis of STING expression was performed using ImageJ according to the provider's instructions (Schneider et al., 2012). To facilitate the identification of malignant

cells and direct quantification, all IHC stains were interpreted in conjunction with H&E-stained sections. This approach can help distinguish tumor cells from immune cells and thus allow reliable PD-L1 immune quantification on different cell subsets as previously established (Herbst et al., 2014; Tumeh et al., 2014; Twyman-Saint Victor et al., 2015).

Small interfering RNA (siRNA) knockdown—Knockdown of c-MYC was achieved using siGENOME Human MYC siRNA SMARTpool at a concentration of 10 nM or sham control obtained by Horizon Discovery (Lafayette, CO).

CRISPR/Cas9 knockout—Knockout of *SMARCB1* was achieved by lentivirus generated in HEK-293FT cells using pLentiCRISPR v2 plasmids harboring gRNA sequences against *SMARCB1* obtained from Genscript (Piscataway, NJ, USA). We used psPAX2, a gift from Didier Trono (Addgene plasmid # 12260 ; http://n2t.net/addgene:12260 ; RRID:Addgene_12260) for lentiviral packaging, as well as pMD2.G, also a gift from Didier Trono (Addgene plasmid # 12259 ; http://n2t.net/addgene:12259 ; RRID:Addgene_12259) for lentiviral envelope expression. Lentiviral transduced cells were selected with puromycin. As negative control, we used cells transduced by lentivirus generated using a pLentiCRISPR v2 plasmid harboring non-targeting control gRNA (BRDN0001145885) (Doench et al., 2016), a gift from John Doench & David Root (Addgene plasmid # 80196 ; http://n2t.net/addgene:80196 ; RRID:Addgene_80196). Propagation of all plasmid vectors was performed using the E. coli strain DH5α (Invitrogen; Cat#18265017).

gRNA target sequences used for human *SMARCB1* knockout:

- TGAGAACGCATCTCAGCCCG
- CATCGATCTCCATGTCCAGC

Non-targeting control gRNA sequence:

- GGGACGCGAAAGAAACCAGT

Immunofluorescence staining—RMC2C and RMC219 cells were plated onto a 6-well culture dish on a coverslip and fixed in 4% paraformaldehyde for 20 minutes, then washed 2 times with PBS. After washing again, cells were permeabilized and stained with a solution of 0.5% Triton X-100 for 15 minutes, then washed 2 times after permeabilization with PBS and blocked for one hour using 3.75% BSA. After blocking, the primary rabbit γH2AX antibody (Cell Signaling Technology; catalogue##2577) was added in 3.75% BSA solution at a ratio of 1:500 and incubated overnight at 4°C. After the overnight incubation, cells were washed 3 times and then incubated for one hour with Alexa Fluor 546 anti-rabbit secondary fluorescent antibody purchased from Invitrogen (Life Technologies). The nuclear content was stained with DAPI reagent (Invitrogen, Life Technologies) for 10 minutes at room temperature. Cells were washed again 3 times with PBS and mounted on a slide using slowfade gold antifade solution (Thermo Fisher Scientific). The corners were sealed using nail polish and images were taken using a Nikon Eclipse Ti2 deconvolution microscope. γH2AX foci within nuclei were quantified using the FindFoci plugin in ImageJ (Herbert et al., 2014).

Chromatin immunoprecipitation sequencing (ChIP)—We analyzed previously published c-MYC chromatin immunoprecipitation sequencing (ChIP-Seq) data from SMARCB1-negative G401 cells expressing tetracycline-inducible enhanced fluorescent protein (EGFP) control or SMARCB1 (Weissmiller et al., 2019). ChIP-seq maps were generated by mapping reads to the human genome GRCh38 using bowtie2 (Langmead and Salzberg, 2012), and visualizing genome-wide maps using the Integrative Genome Viewer software (Thorvaldsdottir et al., 2013). c-MYC peaks were called using MACS2 (Zhang et al., 2008) at an FDR < 0.05. We first determined the union of peaks over the two replicates of each experiment, then determined the lost c-MYC peaks after SMARCB1 re-expression using BEDTOOLS (Quinlan and Hall, 2010). Finally, lost c-MYC peaks were annotated for nearby genes, within a 10 kbp window from the gene body, using BEDTOOLS (Quinlan and Hall, 2010). Enriched pathways were determined using the hypergeometric distribution, with significance achieved at FDR-adjusted p value<0.05 against the Hallmark and REACTOME compendia of pathways (Fabregat et al., 2018; Liberzon et al., 2015).

For the chromatin immunoprecipitation quantitative polymerase chain reaction (ChIP-qPCR) experiments, RMC2C cells expressing tetracycline-inducible SMARCB1 or empty vector control were plated at 10×10^6 cells per plate and treated with 0.5 μg/mL doxycycline for 48 hours. The cells were crosslinked using 0.4% paraformaldehyde for 10 minutes, quenched with 0.125M glycine for 10 minutes, washed with ice-cold PBS two times, and collected by centrifugation. Nuclei were extracted in 50 mM Tris HCl, pH8, 10 mM EDTA, 1% SDS for 15 minutes on ice. Chromatin was fragmented using a Covaris E220 ultrasonicator, and debris were removed by centrifugation. Chromatin was frozen at −80 °C until ready to use. Each immuno-precipitation was performed on chromatin collected from 10×10^6 cells by dilution in 8 volumes of ChIP dilution buffer (16.7 mM Tris HCl, pH 8, 167 mM NaCl, 1.2 mM EDTA, 1.1% Triton, 0.01% SDS) using 5 μg of rabbit polyclonal antibody against c-MYC (Santa Cruz Biotechnology, sc-764) or normal rabbit IgG control (Cell Signaling, 2729; 5 μg). Immunoprecipitated chromatin was bound to protein A Dynabeads (ThermoFisher Scientific) and washed twice sequentially with low salt buffer (20 mM Tris HCl, pH 8, 150 mM NaCl, 2 mM EDTA, 1% Triton, 0.1% SDS), high salt buffer (20 mM Tris HCl, pH 8, 500 mM NaCl, 2mM EDTA, 1% Triton, 0.1% SDS), lithium chloride buffer (10 mM Tris HCl, pH 8, 0.25 M LiCl, 1 mM EDTA, 1% NP-40, 1% sodium deoxycholate) and TE (10 mM Tris HCl, pH 8, 1 mM EDTA). Dynabead-bound chromatin was eluted in 1% SDS and 0.1 M $NaHCO_3$ two times for 15 minutes at room temperature, before being treated with 10μg RNase A overnight at 65 °C. DNA was then decrosslinked with 20μg proteinase K for 1hr at 42 °C before extraction using a classical phenol/chroloform protocol. Samples were diluted in distilled water and quantiied by Q-PCR using the following primers targeting the transcription start sites of each gene:

- *CCNE2* : CAGCACAACGTGGAGTGG and AGAGCAGAGCCGCACTTG
- *CDK4* : ATGTGACCAGCTGCCAAAG and TTACACTCTTCGCCCTCCTC
- *ATF4* : CGAAGGAAAGAACGGACTCTG and TTATGGCCTCACGAAAGGAG)
- *PRM1*: ACAGAGCGACACCCTGTCAT and AGGCGGTGGTTACACAACAT

Chemical compounds—Olaparib, niraparib, VX970, AZD6738, and adavosertib were obtained from Selleckchem (Houston, TX, USA) and dissolved in DMSO. Clinical-grade doxorubicin, gemcitabine, carboplatin, cisplatin, and paclitaxel were obtained from the Department of Pharmacy at The University of Texas MD Anderson Cancer Center (Houston, TX, USA).

Cell viability experiments—Cell viability was determined using the cell proliferation kit 3-(4,5-dimethylthiazol-2-yl)-2,5-diphenyltetrazolium bromide (MTT) colorimetric assay (Sigma-Aldrich). Cells were plated in 96-well plates at a density of 5.0×10^3 cells/well. Twenty-four hours after seeding, the cells were treated with different drug concentrations ranging from 0.01 to 20 μM. The MTT assay was performed at 120 hours after treatment. The cells were incubated with 10% MTT added directly to the medium for 4 hours at 37°C, followed by cell lysis with detergent reagent overnight in the dark at room temperature. Absorbance was determined at 570 nm in three independent wells per condition for each experiment and results are presented as the means of at least three independent experiments. Dose response curves and the half maximal inhibitory concentration (IC_{50}) were calculated using the Dr Fit software (Di Veroli et al., 2015). For all SMARCB1 re-expression cell viability experiments, a doxycycline concentration of 0.5 μg/mL was used for 3 days in cells harboring the tetracycline-inducible pIND20-fSNF5-HA vector or the pInducer20 empty backbone control prior to initiating drug treatments. For siRNA knockdown cell viability experiments, cells were first treated with siRNA against c-MYC or sham control for 72 hours prior to initiating drug treatments. Chemotherapy drug concentrations used for *in vitro* experiments were all chosen to be less than their respective peak plasma concentrations in humans (Ciccolini et al., 2016; Pavlik et al., 1982; Swift and Golsteyn, 2014; Von Hoff et al., 1986).

DNA fiber assay—DNA fiber assays were performed as previously described (Jackson and Pombo, 1998; Schlacher et al., 2011). Briefly, cells were labeled with IdU (50 μM, 25 min), followed by labeling with CldU (50 μM, 25 min) and spread as described before standard detection of IdU and CldU tracts using primary antibodies against anti-IdU / anti-BrdU (mouse monoclonal; BD Biosciences; clone B44, 1:100 in blocking buffer) and anti-CldU / anti-BrdU [rat monoclonal; Santa Cruz Biotechnology; BU1/75(ICR1), sc-56258, 1:200 in blocking buffer], as well as secondary antibodies goat polyclonal anti-mouse Alexa Fluor 488 (ThermoFisher; A-11001, 1:200 in blocking buffer) and goat polyclonal anti-rat Alexa Fluor 555 (ThermoFisher; A-21434, 1:300 in blocking buffer), respectively. Fibers were imaged (Nikon microscope) and analyzed using ImageJ software (Schneider et al., 2012). The rate for nascent tract replication was estimated using the conversion of 2.59 kb/um (Jackson and Pombo, 1998).

***In vivo* treatments—**Studies involving animals, including housing and care, method of euthanasia, and experimental protocols were approved by the University of Texas MD Anderson Cancer Center Animal Care and Use Committee and were in accordance with appropriate guidelines (protocol ACUF 00000884-RN02). To test the *in vivo* efficacy of drugs targeting DDR pathways, CB-17 female scid mice aged 6–9 weeks old and harboring subcutaneous RMC PDX tumors were randomly assigned to one of four treatment groups (n

= 5 mice/group): 1) oral administration of the PARP inhibitor niraparib (50 mg/kg/day) + oral vehicle control (DMSO) once daily, 2) oral administration of the ATR inhibitor AZD6738 (25 mg/kg/day) + oral vehicle control (DMSO) once daily, 3) oral administration of niraparib (50 mg/kg/day) + oral AZD6738 (25 mg/kg/day) once daily, 4) oral administration of only vehicle control (DMSO) once daily. Mice were treated daily for 5 days with 2 days off treatment for a total period of 25 days. For preclinical *in vivo* testing of niraparib alone or in combination with cisplatin, mice were randomly assigned to one of four treatment groups (n = 10 mice/group): 1) Oral administration of niraparib (50 mg/kg/day) once daily + cisplatin 1.25 mg/kg intraperitoneally weekly, 2) oral vehicle control (DMSO) once daily + cisplatin 1.25 mg/kg intraperitoneally weekly, 3) Oral administration of niraparib (50 mg/kg/day) once daily + vehicle control (normal saline) intraperitoneally weekly, 4) oral vehicle control (DMSO) once daily + vehicle control (normal saline) intraperitoneally weekly. Niraparib or oral vehicle control were administered daily for 5 days with 2 days off treatment for a total period of 25 days. Cisplatin or intraperitoneal vehicle control were were administered weekly x3 weeks. Treatments were started when tumor volume reached 100 to 200 mm^3. Tumor volume was measured twice weekly using Vernier calipers and calculated by the formula: volume = [(smallest diameter)^2 × (largest diameter)]/2.

Quantification and Statistical Analysis

All statistical analyses were performed using R (R Core Team, 2019). Continuous measures are presented as the mean ± standard error of the mean of biological replicates. Differences in means between two groups for all *in vitro* experiments were compared using a two-tailed Welch's *t* test unless otherwise specified in the text and figures. The p values for the pathway diagrams in Figures 4E, 4F and 5F were generated using the Wald test. The p values for STING IHC quantification levels in Figure 5E, the ChIP-qPCR in Figure 6G, and the comparisons between DNA fiber tract lengths in Figure 6H were generated using the Mann-Whitney U test. For *in vivo* tumor growth assessment, groups of mice randomized to each treatment (n = 5 per group) were monitored twice weekly. We performed semiparametric ANCOVA by generating proportional odds models using the regression modeling strategies (rms) statistical package in R (version 3.2.3). Regression imputation was used for missing data. A smooth nonlinear relationship was assumed between baseline and final tumor volumes at the end of treatment, using restricted cubic splines with three knots (Harrell, 2015). Power analyses were performed using the popower function in the Hmisc package in R (version 3.2.3). With n = 5 mice per group, we had approximately 80% power at the 0.05 alpha level to detect a difference in tumor volume between two groups by an effect size of 1.875 (Cohen's d) at the end of treatment. With n = 10 mice per group, we had approximately 80% power at the 0.05 alpha level to detect a difference in tumor volume between two groups by an effect size of 1.27 (Cohen's d) at the end of treatment.

Data and Software Availability

Sequencing data generated in this paper have been deposited at the NCBI Sequence Read Archive (SRA) hosted by the NIH (SRA accession: PRJNA605003). Clear cell renal cell carcinoma, papillary renal cell carcinoma, and chromophobe renal cell carcinoma sequencing data were obtained from the Cancer Genome Atlas (https://

portal.gdc.cancer.gov/projects/). Kidney MRT sequencing data were generated by Chun et al. (2016) (dbGaP accession number phs000470.v18.p7). MRT and ATRT sequencing data were generated by Lee et al. (2012) (dbGaP accession number phs000508). G401 c-MYC ChiP-seq data were generated by Weissmiller et al. (2019) (GEO accession number GSE109310).

Supplementary Material

Refer to Web version on PubMed Central for supplementary material.

Acknowledgements

We thank Dr. Waun Ki Hong for discussions and suggestions. We thank Dr. Bernard E. Weissman for discussions and reagents. We thank Dr. Bora Lim for creative assistance with illustrations. We thank the UTMDACC Advanced Technology Genomics Core (ATGC) and the Cytogenetics and Cell Authentication Core. We thank Thomas Huynh and the UTMDACC Department of Veterinary Medicine & Surgery Anatomic Pathology Laboratory. This work was supported in part by the Cancer Center Support Grant to MDACC (grant number P30 CA016672) from the National Cancer Institute of the National Institutes of Health, and by philanthropic donations from the Chris “CJ” Johnson Foundation Inc and R.M.C. Inc. P.M. was supported by a Conquer Cancer Foundation Young Investigator Award, a Kidney Cancer Association Young Investigator Award, a United States Department of Defense Concept Award, and the National Institutes of Health grant T32 CA009666. J.P.B. and B.H.V. were funded by La Ligue Nationale Contre le Cancer. J.P.B. was also supported by the Philip Foundation. I.D. is an ‘équipe labélisée’ of the Ligue Nationale contre le Cancer. S.S. was supported by the CPRIT Research Training Grant (RP170067). C.C. and C.J.C. were supported by the NIH grant CA125123. F.C. is supported by the Italian Association for Cancer Research AIRC for abroad fellowship. R.N.H.S. is supported by an American Heart Association predoctoral fellowship 19PRE34430069. K.S. is supported by grants NIH 1R01ES029680, CPRIT RP180813 and RP180463, and is a Rita Allen Fellow and a CPRIT Scholar in Cancer Biology.

REFERENCES

Alexandrov LB, Jones PH, Wedge DC, Sale JE, Campbell PJ, Nik-Zainal S, and Stratton MR (2015). Clock-like mutational processes in human somatic cells. Nat Genet 47, 1402–1407. [PubMed: 26551669]

Alexandrov LB, Nik-Zainal S, Wedge DC, Aparicio SA, Behjati S, Biankin AV, Bignell GR, Bolli N, Borg A, Borresen-Dale AL, et al. (2013). Signatures of mutational processes in human cancer. Nature 500, 415–421. [PubMed: 23945592]

Alvarez O, Rodriguez MM, Jordan L, and Sarnaik S (2015). Renal medullary carcinoma and sickle cell trait: A systematic review. Pediatr Blood Cancer 62, 1694–1699. [PubMed: 26053587]

Anders S, Pyl PT, and Huber W (2015). HTSeq--a Python framework to work with high-throughput sequencing data. Bioinformatics 31, 166–169. [PubMed: 25260700]

Andrews S (2014). FastQC A Quality Control tool for High Throughput Sequence Data.

Arun G, Diermeier SD, and Spector DL (2018). Therapeutic Targeting of Long Non-Coding RNAs in Cancer. Trends Mol Med 24, 257–277. [PubMed: 29449148]

Aryee MJ, Jaffe AE, Corrada-Bravo H, Ladd-Acosta C, Feinberg AP, Hansen KD, and Irizarry RA (2014). Minfi: a flexible and comprehensive Bioconductor package for the analysis of Infinium DNA methylation microarrays. Bioinformatics 30, 1363–1369. [PubMed: 24478339]

Bakhoum SF, Ngo B, Laughney AM, Cavallo JA, Murphy CJ, Ly P, Shah P, Sriram RK, Watkins TBK, Taunk NK, et al. (2018). Chromosomal instability drives metastasis through a cytosolic DNA response. Nature 553, 467–472. [PubMed: 29342134]

Becht E, Giraldo NA, Lacroix L, Buttard B, Elarouci N, Petitprez F, Selves J, Laurent-Puig P, Sautes-Fridman C, Fridman WH, and de Reynies A (2016). Estimating the population abundance of tissue-infiltrating immune and stromal cell populations using gene expression. Genome Biol 17, 218. [PubMed: 27765066]

Beck H, Nahse V, Larsen MS, Groth P, Clancy T, Lees M, Jorgensen M, Helleday T, Syljuasen RG, and Sorensen CS (2010). Regulators of cyclin-dependent kinases are crucial for maintaining genome integrity in S phase. J Cell Biol 188, 629–638. [PubMed: 20194642]

Becker F, Junker K, Parr M, Hartmann A, Fussel S, Toma M, Grobholz R, Pflugmann T, Wullich B, Strauss A, et al. (2013). Collecting duct carcinomas represent a unique tumor entity based on genetic alterations. PLoS One 8, e78137. [PubMed: 24167600]

Beroukhim R, Mermel CH, Porter D, Wei G, Raychaudhuri S, Donovan J, Barretina J, Boehm JS, Dobson J, Urashima M, et al. (2010). The landscape of somatic copy-number alteration across human cancers. Nature 463, 899–905. [PubMed: 20164920]

Brugarolas J (2014). Molecular genetics of clear-cell renal cell carcinoma. J Clin Oncol 32, 1968–1976. [PubMed: 24821879]

Cajaiba MM, Dyer LM, Geller JI, Jennings LJ, George D, Kirschmann D, Rohan SM, Cost NG, Khanna G, Mullen EA, et al. (2018). The classification of pediatric and young adult renal cell carcinomas registered on the Children's Oncology Group (COG) protocol AREN03B2 after focused genetic testing. Cancer.

Calderaro J, Masliah-Planchon J, Richer W, Maillot L, Maille P, Mansuy L, Bastien C, de la Taille A, Boussion H, Charpy C, et al. (2016). Balanced Translocations Disrupting SMARCB1 Are Hallmark Recurrent Genetic Alterations in Renal Medullary Carcinomas. Eur Urol 69, 1055–1061. [PubMed: 26433572]

Campan M, Weisenberger DJ, Trinh B, and Laird PW (2009). MethyLight. Methods Mol Biol 507, 325–337. [PubMed: 18987824]

Cancer Genome Atlas Research, N. (2013). Comprehensive molecular characterization of clear cell renal cell carcinoma. Nature 499, 43–49. [PubMed: 23792563]

Cancer Genome Atlas Research, N., Linehan WM, Spellman PT, Ricketts CJ, Creighton CJ, Fei SS, Davis C, Wheeler DA, Murray BA, Schmidt L, et al. (2016). Comprehensive Molecular Characterization of Papillary Renal-Cell Carcinoma. N Engl J Med 374, 135–145. [PubMed: 26536169]

Carlo MI, Chaim J, Patil S, Kemel Y, Schram AM, Woo K, Coskey D, Nanjangud GJ, Voss MH, Feldman DR, et al. (2017). Genomic Characterization of Renal Medullary Carcinoma and Treatment Outcomes. Clin Genitourin Cancer 15, e987–e994. [PubMed: 28558987]

Carugo A, Minelli R, Sapio L, Soeung M, Carbone F, Robinson FS, Tepper J, Chen Z, Lovisa S, Svelto M, et al. (2019). p53 Is a Master Regulator of Proteostasis in SMARCB1-Deficient Malignant Rhabdoid Tumors. Cancer Cell 35, 204–220 e209. [PubMed: 30753823]

Cescon DW, and Haibe-Kains B (2016). DNA replication stress: a source of APOBEC3B expression in breast cancer. Genome Biol 17, 202. [PubMed: 27716362]

Chen F, Zhang Y, Gibbons DL, Deneen B, Kwiatkowski DJ, Ittmann M, and Creighton CJ (2018). Pan-Cancer Molecular Classes Transcending Tumor Lineage Across 32 Cancer Types, Multiple Data Platforms, and over 10,000 Cases. Clin Cancer Res 24, 2182–2193. [PubMed: 29440175]

Chen PL, Roh W, Reuben A, Cooper ZA, Spencer CN, Prieto PA, Miller JP, Bassett RL, Gopalakrishnan V, Wani K, et al. (2016). Analysis of Immune Signatures in Longitudinal Tumor Samples Yields Insight into Biomarkers of Response and Mechanisms of Resistance to Immune Checkpoint Blockade. Cancer Discov 6, 827–837. [PubMed: 27301722]

Chen Y, Yao H, Thompson EJ, Tannir NM, Weinstein JN, and Su X (2013). VirusSeq: software to identify viruses and their integration sites using next-generation sequencing of human cancer tissue. Bioinformatics 29, 266–267. [PubMed: 23162058]

Cheval L, Pierrat F, Rajerison R, Piquemal D, and Doucet A (2012). Of mice and men: divergence of gene expression patterns in kidney. PLoS One 7, e46876. [PubMed: 23056504]

Choueiri TK, and Motzer RJ (2017). Systemic Therapy for Metastatic Renal-Cell Carcinoma. N Engl J Med 376, 354–366. [PubMed: 28121507]

Chun HE, Lim EL, Heravi-Moussavi A, Saberi S, Mungall KL, Bilenky M, Carles A, Tse K, Shlafman I, Zhu K, et al. (2016). Genome-Wide Profiles of Extra-cranial Malignant Rhabdoid Tumors Reveal Heterogeneity and Dysregulated Developmental Pathways. Cancer Cell 29, 394–406. [PubMed: 26977886]

Cibulskis K, Lawrence MS, Carter SL, Sivachenko A, Jaffe D, Sougnez C, Gabriel S, Meyerson M, Lander ES, and Getz G (2013). Sensitive detection of somatic point mutations in impure and heterogeneous cancer samples. Nat Biotechnol 31, 213–219. [PubMed: 23396013]

Ciccolini J, Serdjebi C, Peters GJ, and Giovannetti E (2016). Pharmacokinetics and pharmacogenetics of Gemcitabine as a mainstay in adult and pediatric oncology: an EORTC-PAMM perspective. Cancer Chemother Pharmacol 78, 1–12. [PubMed: 27007129]

Ciro M, Prosperini E, Quarto M, Grazini U, Walfridsson J, McBlane F, Nucifero P, Pacchiana G, Capra M, Christensen J, and Helin K (2009). ATAD2 is a novel cofactor for MYC, overexpressed and amplified in aggressive tumors. Cancer Res 69, 8491–8498. [PubMed: 19843847]

Cook SA, and Tinker AV (2019). PARP Inhibitors and the Evolving Landscape of Ovarian Cancer Management: A Review. BioDrugs.

Davis CF, Ricketts CJ, Wang M, Yang L, Cherniack AD, Shen H, Buhay C, Kang H, Kim SC, Fahey CC, et al. (2014). The somatic genomic landscape of chromophobe renal cell carcinoma. Cancer Cell 26, 319–330. [PubMed: 25155756]

Di Veroli GY, Fornari C, Goldlust I, Mills G, Koh SB, Bramhall JL, Richards FM, and Jodrell DI (2015). An automated fitting procedure and software for dose-response curves with multiphasic features. Sci Rep 5, 14701. [PubMed: 26424192]

Do H, and Dobrovic A (2015). Sequence artifacts in DNA from formalin-fixed tissues: causes and strategies for minimization. Clin Chem 61, 64–71. [PubMed: 25421801]

Doench JG, Fusi N, Sullender M, Hegde M, Vaimberg EW, Donovan KF, Smith I, Tothova Z, Wilen C, Orchard R, et al. (2016). Optimized sgRNA design to maximize activity and minimize off-target effects of CRISPR-Cas9. Nat Biotechnol 34, 184–191. [PubMed: 26780180]

Dong Y, Manley BJ, Becerra MF, Redzematovic A, Casuscelli J, Tennenbaum DM, Reznik E, Han S, Benfante N, Chen YB, et al. (2017). Tumor Xenografts of Human Clear Cell Renal Cell Carcinoma But Not Corresponding Cell Lines Recapitulate Clinical Response to Sunitinib: Feasibility of Using Biopsy Samples. Eur Urol Focus 3, 590–598. [PubMed: 28753786]

Durkin SG, and Glover TW (2007). Chromosome fragile sites. Annu Rev Genet 41, 169–192. [PubMed: 17608616]

Fabregat A, Jupe S, Matthews L, Sidiropoulos K, Gillespie M, Garapati P, Haw R, Jassal B, Korninger F, May B, et al. (2018). The Reactome Pathway Knowledgebase. Nucleic Acids Res 46, D649–D655. [PubMed: 29145629]

Favero F, Joshi T, Marquard AM, Birkbak NJ, Krzystanek M, Li Q, Szallasi Z, and Eklund AC (2015). Sequenza: allele-specific copy number and mutation profiles from tumor sequencing data. Ann Oncol 26, 64–70. [PubMed: 25319062]

Forbes SA, Beare D, Boutselakis H, Bamford S, Bindal N, Tate J, Cole CG, Ward S, Dawson E, Ponting L, et al. (2017). COSMIC: somatic cancer genetics at high-resolution. Nucleic Acids Res 45, D777–D783. [PubMed: 27899578]

Frampton GM, Fichtenholtz A, Otto GA, Wang K, Downing SR, He J, Schnall-Levin M, White J, Sanford EM, An P, et al. (2013). Development and validation of a clinical cancer genomic profiling test based on massively parallel DNA sequencing. Nat Biotechnol 31, 1023–1031. [PubMed: 24142049]

Fuller CE (2016). All things rhabdoid and SMARC: An enigmatic exploration with Dr. Louis P. Dehner. Semin Diagn Pathol 33, 427–440. [PubMed: 27745735]

Genovese G, Carugo A, Tepper J, Robinson FS, Li L, Svelto M, Nezi L, Corti D, Minelli R, Pettazzoni P, et al. (2017). Synthetic vulnerabilities of mesenchymal subpopulations in pancreatic cancer. Nature 542, 362–366. [PubMed: 28178232]

Gupta R, Billis A, Shah RB, Moch H, Osunkoya AO, Jochum W, Hes O, Bacchi CE, de Castro MG, Hansel DE, et al. (2012). Carcinoma of the collecting ducts of Bellini and renal medullary carcinoma: clinicopathologic analysis of 52 cases of rare aggressive subtypes of renal cell carcinoma with a focus on their interrelationship. Am J Surg Pathol 36, 1265–1278. [PubMed: 22895263]

Ha G, Roth A, Lai D, Bashashati A, Ding J, Goya R, Giuliany R, Rosner J, Oloumi A, Shumansky K, et al. (2012). Integrative analysis of genome-wide loss of heterozygosity and monoallelic

expression at nucleotide resolution reveals disrupted pathways in triple-negative breast cancer. Genome Res 22, 1995–2007. [PubMed: 22637570]

Harrell FEJ (2015). Regression Modeling Strategies, Second edn: Springer-Verlag.

Harrow J, Frankish A, Gonzalez JM, Tapanari E, Diekhans M, Kokocinski F, Aken BL, Barrell D, Zadissa A, Searle S, et al. (2012). GENCODE: the reference human genome annotation for The ENCODE Project. Genome Res 22, 1760–1774. [PubMed: 22955987]

Hasselblatt M, Isken S, Linge A, Eikmeier K, Jeibmann A, Oyen F, Nagel I, Richter J, Bartelheim K, Kordes U, et al. (2013). High-resolution genomic analysis suggests the absence of recurrent genomic alterations other than SMARCB1 aberrations in atypical teratoid/rhabdoid tumors. Genes Chromosomes Cancer 52, 185–190. [PubMed: 23074045]

Hayashi T, Gust KM, Wyatt AW, Goriki A, Jager W, Awrey S, Li N, Oo HZ, Altamirano-Dimas M, Buttyan R, et al. (2016). Not all NOTCH Is Created Equal: The Oncogenic Role of NOTCH2 in Bladder Cancer and Its Implications for Targeted Therapy. Clin Cancer Res 22, 2981–2992. [PubMed: 26769750]

Herbert AD, Carr AM, and Hoffmann E (2014). FindFoci: a focus detection algorithm with automated parameter training that closely matches human assignments, reduces human inconsistencies and increases speed of analysis. PLoS One 9, e114749. [PubMed: 25478967]

Herbst RS, Soria JC, Kowanetz M, Fine GD, Hamid O, Gordon MS, Sosman JA, McDermott DF, Powderly JD, Gettinger SN, et al. (2014). Predictive correlates of response to the anti-PD-L1 antibody MPDL3280A in cancer patients. Nature 515, 563–567. [PubMed: 25428504]

Huang da W, Sherman BT, and Lempicki RA (2009a). Bioinformatics enrichment tools: paths toward the comprehensive functional analysis of large gene lists. Nucleic Acids Res 37, 1–13. [PubMed: 19033363]

Huang da W, Sherman BT, and Lempicki RA (2009b). Systematic and integrative analysis of large gene lists using DAVID bioinformatics resources. Nat Protoc 4, 44–57. [PubMed: 19131956]

Jackson DA, and Pombo A (1998). Replicon Clusters are Stable Units of Chromosome Structure: Evidence That Nuclear Organization Contributes to the Efficient Activation and Propagation of S Phase in Human Cells. The Journal of cell biology 140, 1285–1295. [PubMed: 9508763]

Jalali GR, Vorstman JA, Errami A, Vijzelaar R, Biegel J, Shaikh T, and Emanuel BS (2008). Detailed analysis of 22q11.2 with a high density MLPA probe set. Hum Mutat 29, 433–440. [PubMed: 18033723]

Jia L, Carlo MI, Khan H, Nanjangud GJ, Rana S, Cimera R, Zhang Y, Hakimi AA, Verma AK, Al-Ahmadie HA, et al. (2019). Distinctive mechanisms underlie the loss of SMARCB1 protein expression in renal medullary carcinoma: morphologic and molecular analysis of 20 cases. Mod Pathol.

Kadoch C, and Crabtree GR (2015). Mammalian SWI/SNF chromatin remodeling complexes and cancer: Mechanistic insights gained from human genomics. Sci Adv 1, e1500447. [PubMed: 26601204]

Karam JA, Zhang XY, Tamboli P, Margulis V, Wang H, Abel EJ, Culp SH, and Wood CG (2011). Development and characterization of clinically relevant tumor models from patients with renal cell carcinoma. Eur Urol 59, 619–628. [PubMed: 21167632]

Kerrigan L, and Nims RW (2011). Authentication of human cell-based products: the role of a new consensus standard. Regen Med 6, 255–260. [PubMed: 21391858]

Kim MP, Evans DB, Wang H, Abbruzzese JL, Fleming JB, and Gallick GE (2009). Generation of orthotopic and heterotopic human pancreatic cancer xenografts in immunodeficient mice. Nat Protoc 4, 1670–1680. [PubMed: 19876027]

Kumar R, Nagpal G, Kumar V, Usmani SS, Agrawal P, and Raghava GPS (2019). HumCFS: a database of fragile sites in human chromosomes. BMC Genomics 19, 985. [PubMed: 30999860]

Langmead B, and Salzberg SL (2012). Fast gapped-read alignment with Bowtie 2. Nat Methods 9, 357–359. [PubMed: 22388286]

Lee RS, Stewart C, Carter SL, Ambrogio L, Cibulskis K, Sougnez C, Lawrence MS, Auclair D, Mora J, Golub TR, et al. (2012). A remarkably simple genome underlies highly malignant pediatric rhabdoid cancers. J Clin Invest 122, 2983–2988. [PubMed: 22797305]

Lee WP, Stromberg MP, Ward A, Stewart C, Garrison EP, and Marth GT (2014). MOSAIK: a hash-based algorithm for accurate next-generation sequencing short-read mapping. PLoS One 9, e90581. [PubMed: 24599324]

Leruste A, Tosello J, Ramos RN, Tauziede-Espariat A, Brohard S, Han ZY, Beccaria K, Andrianteranagna M, Caudana P, Nikolic J, et al. (2019). Clonally Expanded T Cells Reveal Immunogenicity of Rhabdoid Tumors. Cancer Cell 36, 597–612 e598. [PubMed: 31708437]

Liberzon A, Birger C, Thorvaldsdottir H, Ghandi M, Mesirov JP, and Tamayo P (2015). The Molecular Signatures Database (MSigDB) hallmark gene set collection. Cell Syst 1, 417–425. [PubMed: 26771021]

Loughery J, Cox M, Smith LM, and Meek DW (2014). Critical role for p53-serine 15 phosphorylation in stimulating transactivation at p53-responsive promoters. Nucleic Acids Res 42, 7666–7680. [PubMed: 24928858]

Love MI, Huber W, and Anders S (2014). Moderated estimation of fold change and dispersion for RNA-seq data with DESeq2. Genome Biol 15, 550. [PubMed: 25516281]

Luthra R, Patel KP, Routbort MJ, Broaddus RR, Yau J, Simien C, Chen W, Hatfield DZ, Medeiros LJ, and Singh RR (2017). A Targeted High-Throughput Next-Generation Sequencing Panel for Clinical Screening of Mutations, Gene Amplifications, and Fusions in Solid Tumors. J Mol Diagn 19, 255–264. [PubMed: 28017569]

Marth GT, Korf I, Yandell MD, Yeh RT, Gu Z, Zakeri H, Stitziel NO, Hillier L, Kwok PY, and Gish WR (1999). A general approach to single-nucleotide polymorphism discovery. Nat Genet 23, 452–456. [PubMed: 10581034]

Maya-Mendoza A, Moudry P, Merchut-Maya JM, Lee M, Strauss R, and Bartek J (2018). High speed of fork progression induces DNA replication stress and genomic instability. Nature 559, 279–284. [PubMed: 29950726]

Meerbrey KL, Hu G, Kessler JD, Roarty K, Li MZ, Fang JE, Herschkowitz JI, Burrows AE, Ciccia A, Sun T, et al. (2011). The pINDUCER lentiviral toolkit for inducible RNA interference in vitro and in vivo. Proc Natl Acad Sci U S A 108, 3665–3670. [PubMed: 21307310]

Mermel CH, Schumacher SE, Hill B, Meyerson ML, Beroukhim R, and Getz G (2011). GISTIC2.0 facilitates sensitive and confident localization of the targets of focal somatic copy-number alteration in human cancers. Genome Biol 12, R41. [PubMed: 21527027]

Mi H, Muruganujan A, and Thomas PD (2013). PANTHER in 2013: modeling the evolution of gene function, and other gene attributes, in the context of phylogenetic trees. Nucleic Acids Res 41, D377–386. [PubMed: 23193289]

Msaouel P, Hong AL, Mullen EA, Atkins MB, Walker CL, Lee CH, Carden MA, Genovese G, Linehan WM, Rao P, et al. (2019). Updated Recommendations on the Diagnosis, Management, and Clinical Trial Eligibility Criteria for Patients With Renal Medullary Carcinoma. Clin Genitourin Cancer 17, 1–6. [PubMed: 30287223]

Msaouel P, Tannir NM, and Walker CL (2018). A Model Linking Sickle Cell Hemoglobinopathies and SMARCB1 Loss in Renal Medullary Carcinoma. Clin Cancer Res 24, 2044–2049. [PubMed: 29440190]

Olshen AB, Venkatraman ES, Lucito R, and Wigler M (2004). Circular binary segmentation for the analysis of array-based DNA copy number data. Biostatistics 5, 557–572. [PubMed: 15475419]

Parra ER, Behrens C, Rodriguez-Canales J, Lin H, Mino B, Blando J, Zhang J, Gibbons DL, Heymach JV, Sepesi B, et al. (2016). Image Analysis-based Assessment of PD-L1 and Tumor-Associated Immune Cells Density Supports Distinct Intratumoral Microenvironment Groups in Non-small Cell Lung Carcinoma Patients. Clin Cancer Res 22, 6278–6289. [PubMed: 27252415]

Pavlik EJ, van Nagell JR Jr., Hanson MB, Donaldson ES, Powell DE, and Kenady DE (1982). Sensitivity to anticancer agents in vitro: standardizing the cytotoxic response and characterizing the sensitivities of a reference cell line. Gynecol Oncol 14, 243–261. [PubMed: 7129221]

Pawel BR (2018). SMARCB1-deficient Tumors of Childhood: A Practical Guide. Pediatr Dev Pathol 21, 6–28. [PubMed: 29280680]

Quinlan AR, and Hall IM (2010). BEDTools: a flexible suite of utilities for comparing genomic features. Bioinformatics 26, 841–842. [PubMed: 20110278]

R Core Team (2019). R: A Language and Environment for Statistical Computing. In, (Vienna, Austria: R Foundation for Statistical Computing).

Schlacher K, Christ N, Siaud N, Egashira A, Wu H, and Jasin M (2011). Double-strand break repair-independent role for BRCA2 in blocking stalled replication fork degradation by MRE11. Cell 145, 529–542. [PubMed: 21565612]

Schneider CA, Rasband WS, and Eliceiri KW (2012). NIH Image to ImageJ: 25 years of image analysis. Nat Methods 9, 671–675. [PubMed: 22930834]

Seiler M, Peng S, Agrawal AA, Palacino J, Teng T, Zhu P, Smith PG, Cancer Genome Atlas Research, N., Buonamici S, and Yu L (2018). Somatic Mutational Landscape of Splicing Factor Genes and Their Functional Consequences across 33 Cancer Types. Cell Rep 23, 282–296 e284. [PubMed: 29617667]

Shah AY, Karam JA, Malouf GG, Rao P, Lim ZD, Jonasch E, Xiao L, Gao J, Vaishampayan UN, Heng DY, et al. (2017). Management and outcomes of patients with renal medullary carcinoma: a multicentre collaborative study. BJU Int 120, 782–792. [PubMed: 27860149]

Stojanova A, Tu WB, Ponzielli R, Kotlyar M, Chan PK, Boutros PC, Khosravi F, Jurisica I, Raught B, and Penn LZ (2016). MYC interaction with the tumor suppressive SWI/SNF complex member INI1 regulates transcription and cellular transformation. Cell Cycle 15, 1693–1705. [PubMed: 27267444]

Subramanian A, Tamayo P, Mootha VK, Mukherjee S, Ebert BL, Gillette MA, Paulovich A, Pomeroy SL, Golub TR, Lander ES, and Mesirov JP (2005). Gene set enrichment analysis: a knowledge-based approach for interpreting genome-wide expression profiles. Proc Natl Acad Sci U S A 102, 15545–15550. [PubMed: 16199517]

Swift LH, and Golsteyn RM (2014). Genotoxic anti-cancer agents and their relationship to DNA damage, mitosis, and checkpoint adaptation in proliferating cancer cells. Int J Mol Sci 15, 3403–3431. [PubMed: 24573252]

Takita J, Chen Y, Kato M, Ohki K, Sato Y, Ohta S, Sugita K, Nishimura R, Hoshino N, Seki M, et al. (2014). Genome-wide approach to identify second gene targets for malignant rhabdoid tumors using high-density oligonucleotide microarrays. Cancer Sci 105, 258–264. [PubMed: 24418192]

The Bioconductor Dev Team (2014). BSgenome.Hsapiens.UCSC.hg19: Full genome sequences for Homo sapiens (UCSC version hg19). . In

Thorvaldsdottir H, Robinson JT, and Mesirov JP (2013). Integrative Genomics Viewer (IGV): high-performance genomics data visualization and exploration. Brief Bioinform 14, 178–192. [PubMed: 22517427]

Tijhuis AE, Johnson SC, and McClelland SE (2019). The emerging links between chromosomal instability (CIN), metastasis, inflammation and tumour immunity. Mol Cytogenet 12, 17. [PubMed: 31114634]

Triche TJ Jr., Weisenberger DJ, Van Den Berg D, Laird PW, and Siegmund KD (2013). Low-level processing of Illumina Infinium DNA Methylation BeadArrays. Nucleic Acids Res 41, e90. [PubMed: 23476028]

Tseng YY, Moriarity BS, Gong W, Akiyama R, Tiwari A, Kawakami H, Ronning P, Reuland B, Guenther K, Beadnell TC, et al. (2014). PVT1 dependence in cancer with MYC copy-number increase. Nature 512, 82–86. [PubMed: 25043044]

Tumeh PC, Harview CL, Yearley JH, Shintaku IP, Taylor EJ, Robert L, Chmielowski B, Spasic M, Henry G, Ciobanu V, et al. (2014). PD-1 blockade induces responses by inhibiting adaptive immune resistance. Nature 515, 568–571. [PubMed: 25428505]

Twyman-Saint Victor C, Rech AJ, Maity A, Rengan R, Pauken KE, Stelekati E, Benci JL, Xu B, Dada H, Odorizzi PM, et al. (2015). Radiation and dual checkpoint blockade activate non-redundant immune mechanisms in cancer. Nature 520, 373–377. [PubMed: 25754329]

Vaser R, Adusumalli S, Leng SN, Sikic M, and Ng PC (2016). SIFT missense predictions for genomes. Nat Protoc 11, 1–9. [PubMed: 26633127]

Von Hoff DD, Clark GM, Weiss GR, Marshall MH, Buchok JB, Knight WA 3rd, and LeMaistre CF (1986). Use of in vitro dose response effects to select antineoplastics for high-dose or regional administration regimens. J Clin Oncol 4, 1827–1834. [PubMed: 2431110]

Wang XS, Zhang Z, Wang HC, Cai JL, Xu QW, Li MQ, Chen YC, Qian XP, Lu TJ, Yu LZ, et al. (2006). Rapid identification of UCA1 as a very sensitive and specific unique marker for human bladder carcinoma. Clin Cancer Res 12, 4851–4858. [PubMed: 16914571]

Wei D, Goldfarb D, Song S, Cannon C, Yan F, Sakellariou-Thompson D, Emanuele M, Major MB, Weissman BE, and Kuwahara Y (2014). SNF5/INI1 deficiency redefines chromatin remodeling complex composition during tumor development. Mol Cancer Res 12, 1574–1585. [PubMed: 25009291]

Weissmiller AM, Wang J, Lorey SL, Howard GC, Martinez E, Liu Q, and Tansey WP (2019). Inhibition of MYC by the SMARCB1 tumor suppressor. Nat Commun 10, 2014. [PubMed: 31043611]

Xu K, Ma H, McCown TJ, Verma IM, and Kafri T (2001). Generation of a stable cell line producing high-titer self-inactivating lentiviral vectors. Mol Ther 3, 97–104. [PubMed: 11162316]

Yang W, Soares J, Greninger P, Edelman EJ, Lightfoot H, Forbes S, Bindal N, Beare D, Smith JA, Thompson IR, et al. (2013). Genomics of Drug Sensitivity in Cancer (GDSC): a resource for therapeutic biomarker discovery in cancer cells. Nucleic Acids Res 41, D955–961. [PubMed: 23180760]

Young MD, Mitchell TJ, Vieira Braga FA, Tran MGB, Stewart BJ, Ferdinand JR, Collord G, Botting RA, Popescu DM, Loudon KW, et al. (2018). Single-cell transcriptomes from human kidneys reveal the cellular identity of renal tumors. Science 361, 594–599. [PubMed: 30093597]

Zeman MK, and Cimprich KA (2014). Causes and consequences of replication stress. Nat Cell Biol 16, 2–9. [PubMed: 24366029]

Zhang J, Dai Q, Park D, and Deng X (2016). Targeting DNA Replication Stress for Cancer Therapy. Genes (Basel) 7.

Zhang J, Fujimoto J, Zhang J, Wedge DC, Song X, Zhang J, Seth S, Chow CW, Cao Y, Gumbs C, et al. (2014). Intratumor heterogeneity in localized lung adenocarcinomas delineated by multiregion sequencing. Science 346, 256–259. [PubMed: 25301631]

Zhang Y, Liu T, Meyer CA, Eeckhoute J, Johnson DS, Bernstein BE, Nusbaum C, Myers RM, Brown M, Li W, and Liu XS (2008). Model-based analysis of ChIP-Seq (MACS). Genome Biol 9, R137. [PubMed: 18798982]

HIGHLIGHTS

- The molecular profile of RMC distinguishes it from other renal malignancies.
- RMC harbors a high number of focal chromosomal alterations.
- RMC has a distinct immune profile characterized by upregulation of cGAS-STING.
- DNA replication stress is a hallmark of RMC that can be therapeutically targeted.

SIGNIFICANCE

Renal medullary carcinoma (RMC) is a highly aggressive malignancy with poor prognosis that predominantly afflicts young people of African descent. Effective treatment strategies are needed for RMC as less than 5% of patients survive beyond 3 years despite best available therapies. We comprehensively profiled a multi-institutional patient cohort of previously untreated primary RMC tumor samples and identified molecular and immune hallmarks that distinguish RMC from other closely related malignancies and can be therapeutically exploited. Our results provide insights into RMC biology and pave the way to clinical trials for this lethal disease.

Figure 1: Somatic Genomic Alterations in RMC

Oncoplot showing the clinical characteristics, assays used, the number and types of somatic single-nucleotide variations (SNVs), as well as selected genomic alterations detected in renal medullary carcinoma (RMC) samples. Each column represents a different patient. CR, complete response with long term remission following perioperative chemotherapy and nephrectomy; FFPE, formalin-fixed, paraffin-embedded; PR, partial response by the Response Evaluation Criteria in Solid Tumors (RECIST) 1.1; SD, stable disease by RECIST 1.1; PD, progressive disease by RECIST 1.1; PDX, patient-derived xenograft. See also Figure S1 and Table S1.

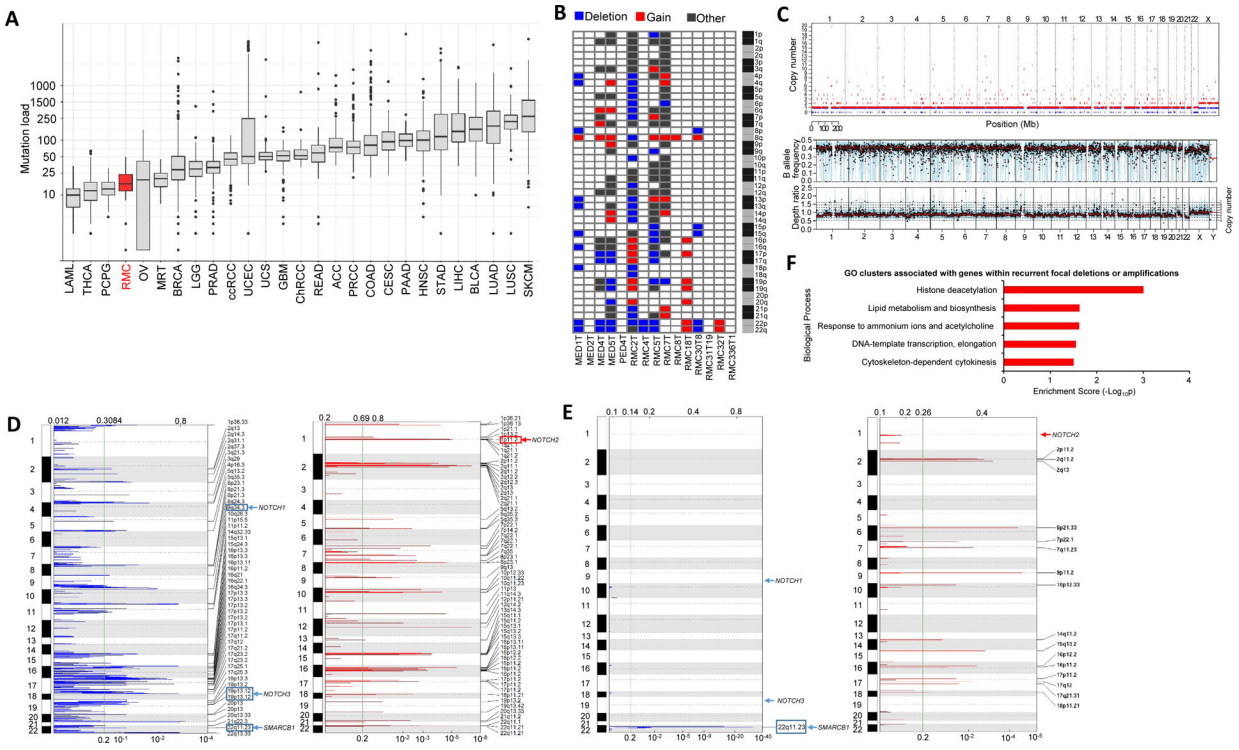

Figure 2: Mutational and Copy Number Landscape of RMC

(A) Tukey boxplots of non-synonymous mutation load per genome for different tumor types. Tumor types are ordered by their median mutation load. RMC samples are highlighted in red. For each boxplot, the central rectangle spans the interquartile range (IQR), the segment within the rectangle shows the median, and the upper and lower whiskers respectively extend the upper and lower hinges of the rectangle by 1.5 * IQR. Black dots represent outliers outside 1.5 * IQR from each hinge. Abbreviations are detailed in the STAR Methods sections. **(B)** Arm-level copy number alterations in untreated primary RMC tumors. Blue corresponds to loss of one copy, red corresponds to a gain, and dark gray corresponds to more complex alterations shown in detail in Figure S2. **(C)** Genome plot of RMC4T. In the bottom two panels, the thick black line indicates the median value, blue bars indicate the interquartile range, and red lines indicate segmented values. Loss of heterozygosity is noted on chromosome 22 encompassing the *SMARCB1* locus. **(D & E)** Regions of focal deletion (left) and amplification (right) identified by GISTIC analysis in untreated primary RMC **(D)** and rhabdoid **(E)** tumors. G-scores (top X axis) and q values (bottom X axis) are shown. Regions with q values of less than 0.20 (as delineated by the vertical green line) are considered to be significantly aberrant. Only focal copy number alterations (shorter than half the length of a chromosome arm) are shown. **(F)** Gene Ontology (GO) analysis of genes within regions of recurrent copy number alterations in RMC. See also Figure S1–S3, and Table S2.

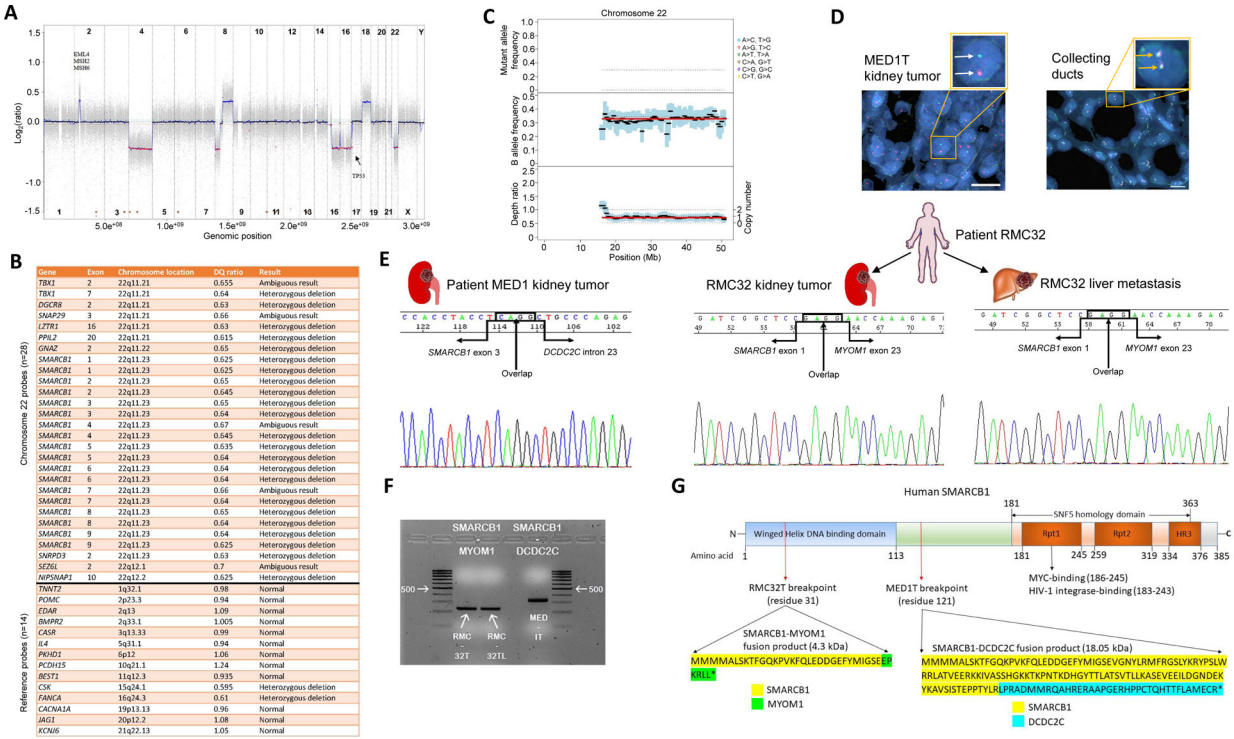

Gene	Exon	Chromosome location	DQ ratio	Result
TBX1	2	22q11.21	0.655	Ambiguous result
TBX1	7	22q11.21	0.64	Heterozygous deletion
DGCR8	2	22q11.21	0.63	Heterozygous deletion
SNAP29	3	22q11.21	0.66	Ambiguous result
LZTR1	16	22q11.21	0.63	Heterozygous deletion
PPIL2	20	22q11.21	0.615	Heterozygous deletion
GNAZ	2	22q11.22	0.65	Heterozygous deletion
SMARCB1	1	22q11.23	0.625	Heterozygous deletion
SMARCB1	1	22q11.23	0.625	Heterozygous deletion
SMARCB1	2	22q11.23	0.65	Heterozygous deletion
SMARCB1	2	22q11.23	0.645	Heterozygous deletion
SMARCB1	3	22q11.23	0.55	Heterozygous deletion
SMARCB1	3	22q11.23	0.64	Heterozygous deletion
SMARCB1	4	22q11.23	0.67	Ambiguous result
SMARCB1	4	22q11.23	0.645	Heterozygous deletion
SMARCB1	5	22q11.23	0.635	Heterozygous deletion
SMARCB1	5	22q11.23	0.64	Heterozygous deletion
SMARCB1	6	22q11.23	0.64	Heterozygous deletion
SMARCB1	6	22q11.23	0.64	Heterozygous deletion
SMARCB1	7	22q11.23	0.66	Ambiguous result
SMARCB1	7	22q11.23	0.64	Heterozygous deletion
SMARCB1	8	22q11.23	0.65	Heterozygous deletion
SMARCB1	8	22q11.23	0.64	Heterozygous deletion
SMARCB1	9	22q11.23	0.64	Heterozygous deletion
SMARCB1	9	22q11.23	0.625	Heterozygous deletion
SNRPD3	2	22q11.23	0.63	Heterozygous deletion
SEZ6L	2	22q12.1	0.7	Ambiguous result
NIPSNAP1	10	22q12.2	0.625	Heterozygous deletion
TNNT2		1q32.1	0.98	Normal
POMC		2p23.3	0.94	Normal
EDAR		2q13	1.09	Normal
BMPR2		2q33.1	1.005	Normal
CASR		3q13.33	0.99	Normal
IL4		5q31.1	0.94	Normal
PKHD1		6p12	1.06	Normal
PCDH15		10q21.1	1.24	Normal
BEST1		11q12.3	0.935	Normal
CSK		15q24.1	0.595	Heterozygous deletion
FANCA		16q24.3	0.61	Heterozygous deletion
CACNA1A		19p13.13	0.96	Normal
JAG1		20p12.2	1.08	Normal
KCNJ6		21q22.13	1.05	Normal

Chromosome 22 probes (n=28)
Reference probes (n=14)

Figure 3: Integrative Characterization of the Mechanisms of SMARCB1 Loss

(A) WES chromosome plot showing chromosome 22 monosomy in sample MED1T. In the bottom two panels, the thick black line indicates the median value, blue bars indicate the interquartile range, and red lines indicate segmented values. **(B)** MLPA analysis of MED1T confirmed the heterozygous deletion present around the *SMARCB1* locus. The heterozygous deletions noted on chromosomes 15 and 16 (CSK and FANCA probes, respectively) were also detected in the WES analysis (Figure S2). **(C)** CGH profile of MED1T. **(D)** Break-apart FISH of MED1T confirmed the presence of chromosome 22 monosomy and revealed the presence of a disruptive translocation around the *SMARCB1* locus as shown by the separation of the green and orange probes (white arrows) seen inside RMC tumor cells (left image). Two yellow fusion signals (yellow arrows) representing two intact *SMARCB1* alleles are noted within the nuclei of normal kidney cells (right image). Scale bar: 10 μm. **(E)** Sanger sequencing confirmation of the fusion RNA product between exon 3 of *SMARCB1* and intron 23 of *DCDC2C* in the MED1T sample (untreated primary tumor), and of the fusion RNA product exon 1 of *SMARCB1* and exon 23 of *MYOM1* on both untreated primary tumor (RMC32T) and untreated liver metastasis (RMC32TL) from patient RMC32. **(F)** Agarose gel electrophoresis of the SMARCB1 fusion products using cDNA from samples RMC32T, RMC32TL, and MED1T. **(G)** Predicted amino acid sequences of the SMARCB1-DCDC2C fusion product in patient MED1 and of the SMARCB1-MYOM1 fusion product in patient RMC32. See also Table S3.

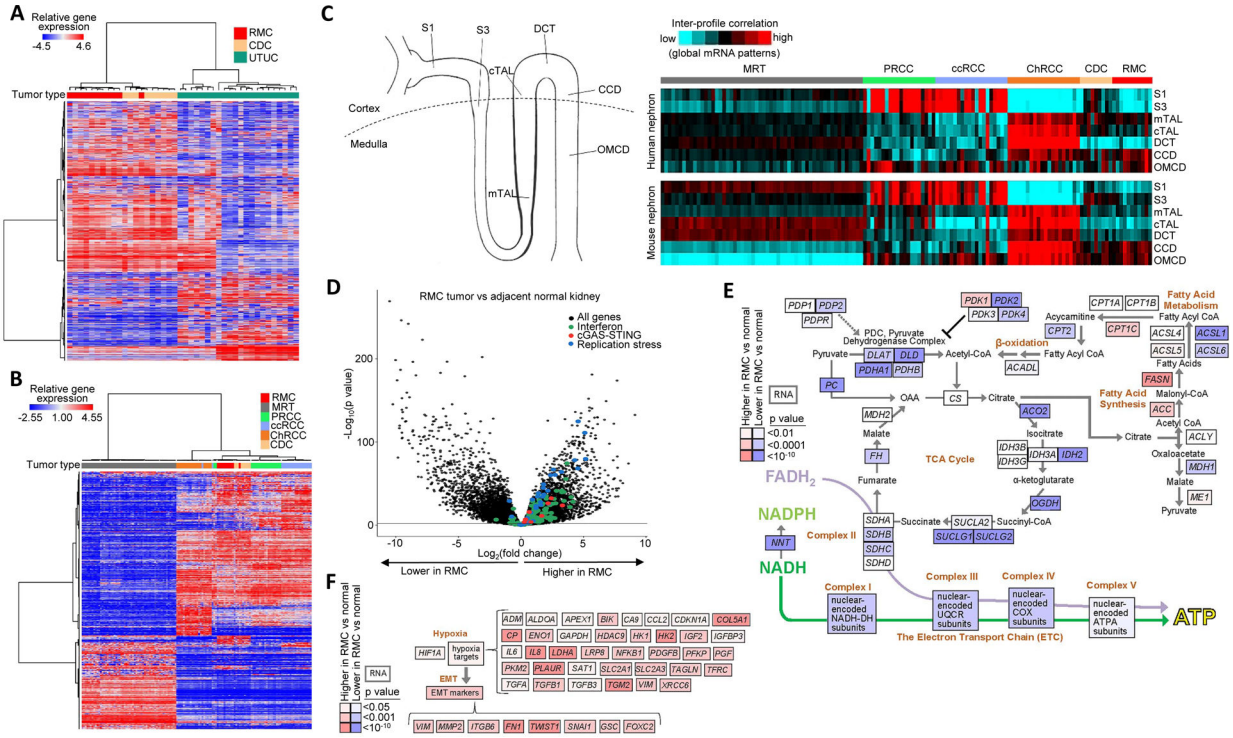

Figure 4: Transcriptomic Signature Distinguishes RMC from Other Renal Malignancies

(A) Unsupervised hierarchical clustering of protein-coding gene expression from RMC, CDC, and UTUC. **(B)** Unsupervised hierarchical clustering of protein-coding gene expression from kidney malignancies. **(C)** A cartoon of the nephron regions (left; the dashed line separates the renal cortex from the medulla) and heat maps (right) showing intersample correlations (Pearson's r) between expression profiles of kidney malignancies (arranged by subtype) and expression profiles of kidney nephron sites. S1 and S3, initial and terminal portions of the proximal tubule; mTAL, medullary thick ascending limb of Henle's loop; cTAL, cortical thick ascending limb of Henle's loop; DCT, distal convoluted tubule; CCD, cortical collecting duct; OMCD, outer medullary collecting duct. **(D)** Volcano plot showing the differential expression of genes involved in replication stress and innate immunity (interferon signaling and cGAS-STING pathways). The secondary horizontal line corresponds to a p value of 0.01. **(E & F)** Pathway diagrams representing differential expression patterns in core metabolic pathways **(E)**, as well as hypoxia-induced genes and EMT **(F)** between RMC tissues and adjacent normal kidney. See also Figure S3, Figure S4, and Table S2, S4.

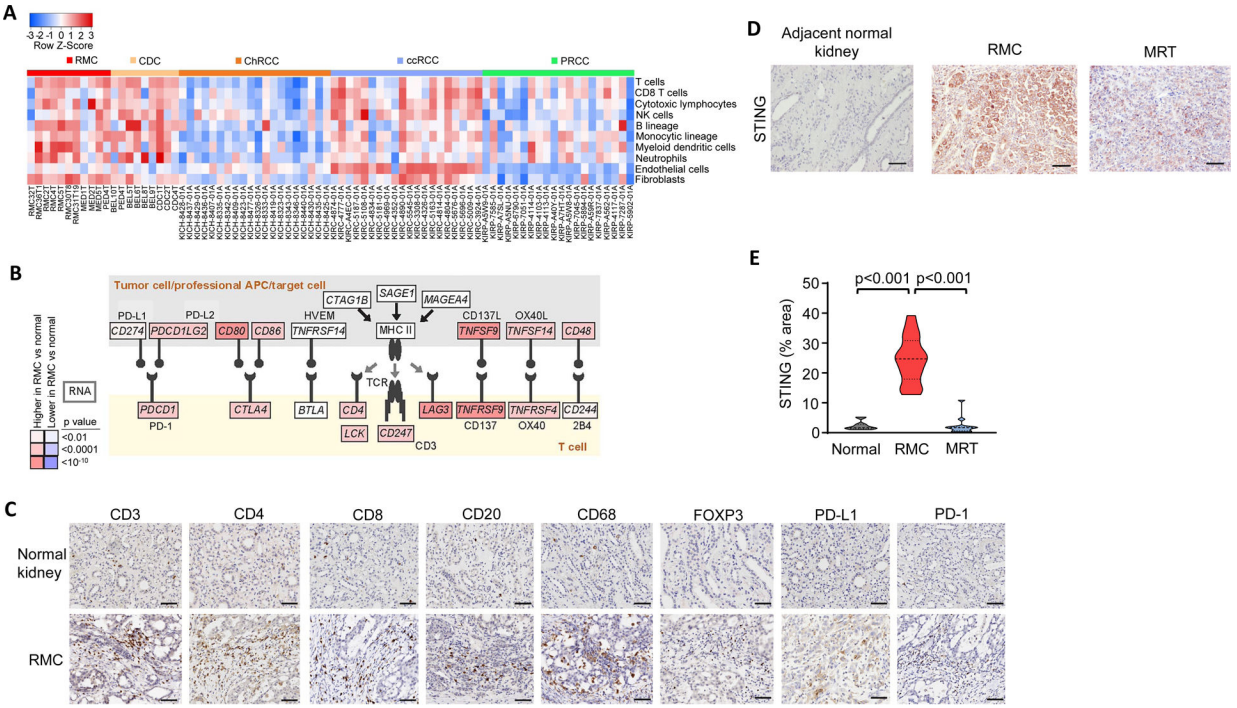

Figure 5: RMC has a Distinct Immune Profile

(A) MCP-counter estimates of infiltrating immune and stromal cells in RMC compared with other carcinomas of the kidney. **(B)** Immune checkpoint pathway diagram showcasing the interactions of T cells with tumor cells and professional antigen-presenting cells based on the differential RNA expression patterns between RMC tumors and adjacent normal kidney tissues. **(C)** Representative immunohistochemistry microphotographs for CD3, CD4, CD8, CD20, CD68, FOXp3, PD-L1, and PD-1 in RMC tumor tissues and adjacent normal collecting tubules. Scale bar: 50 μm. **(D)** Representative immunohistochemistry microphotographs for STING in RMC tumor tissues, adjacent normal collecting tubules, and MRT tumor tissues. Scale bar: 50 μm. **(E)** Violin plots of the IHC quantification levels for STING in RMC tumor tissues (n = 20), adjacent normal kidney (n = 12) and MRT tumor tissues (n = 12). The width of each violin plot is proportional to the density of observed data points in each region. Dashed and dotted lines correspond to the median and interquartile values, respectively. The upper and lower lines correspond to the highest and lowest observed values, respectively. See also Figure S5 and Table S4, S5.

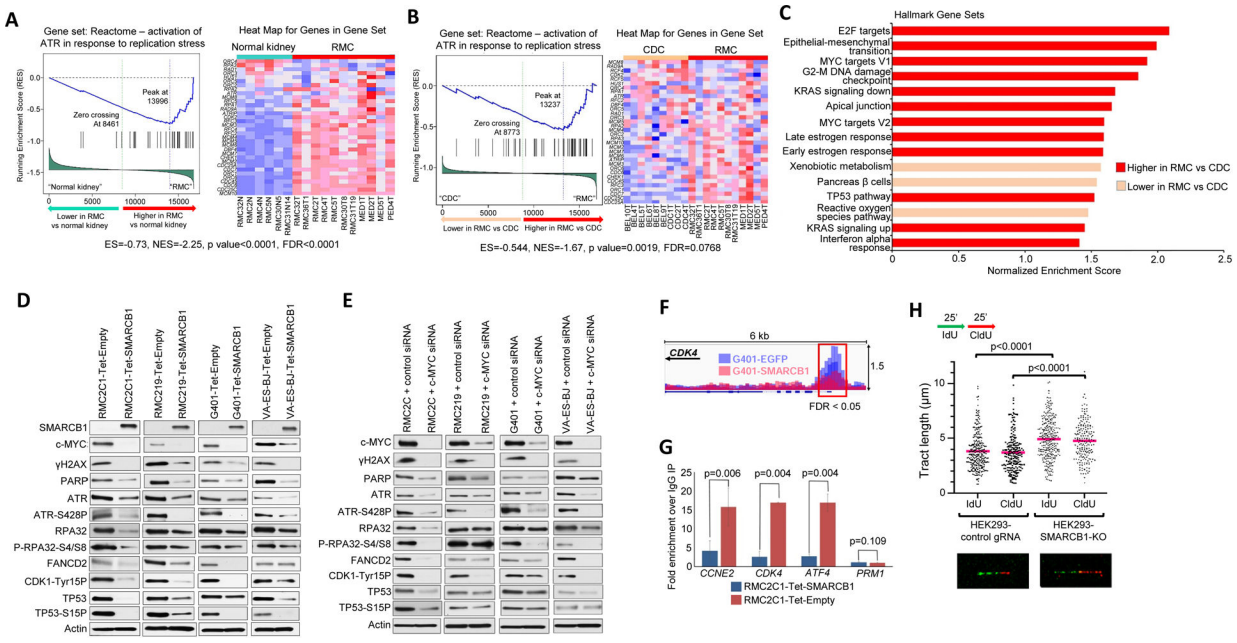

Figure 6: SMARCB1 Loss Promotes MYC-induced Replication Stress

GSEA revealed a significant enrichment for the ATR DNA damage repair pathway in response to replication stress in RMC compared with **(A)** adjacent normal kidney tissues or **(B)** CDC. ES, enrichment score; NES, normalized enrichment score; FDR, false discovery rate. **(C)** Hallmark pathways significantly altered (FDR < 0.1) between RMC and CDC by GSEA analysis. **(D & E)** Western blots of replication stress and DNA damage response pathways following SMARCB1 rescue **(D)** or direct siRNA inhibition of c-MYC **(E)** in RMC2C, RMC219, and other SMARCB1-negative cell lines (G401 and VA-ES-BJ). **(F)** c-MYC peak differences on the promoter site (boxed in red) of the *CDK4* gene in G401 MRT cells re-expressing SMARCB1 or EGFP control. The y-axis represents ChIP-seq read counts normalized to 1 million mapped reads. **(G)** Fold enrichment in c-MYC relative to negative control (normal rabbit IgG) and normalized with input DNA in RMC2C cells following re-expression of SMARCB1 or empty vector control. *CCNE2*, *CDK4*, and *ATF4* are established c-MYC transcriptional targets, whereas *PRM1* is a spermatogenesis-specific gene that is not regulated by c-MYC and serves as negative control. The values are expressed as mean fold change +/− SEM from triplicates. **(H)** Dot plot of DNA fiber tract lengths indicating a replication speed of ~0.39 kb/min in HEK293-control gRNA cells compared with ~0.51 kb/min in *SMARCB1* knock-out cells. Bars (pink) represents the mean of replication tracts (n=187–291, from biological replicas). Top, experimental labeling scheme. Bottom, representative fibers (original magnification x40). See also Figure S6, Table S4, and Table S6.

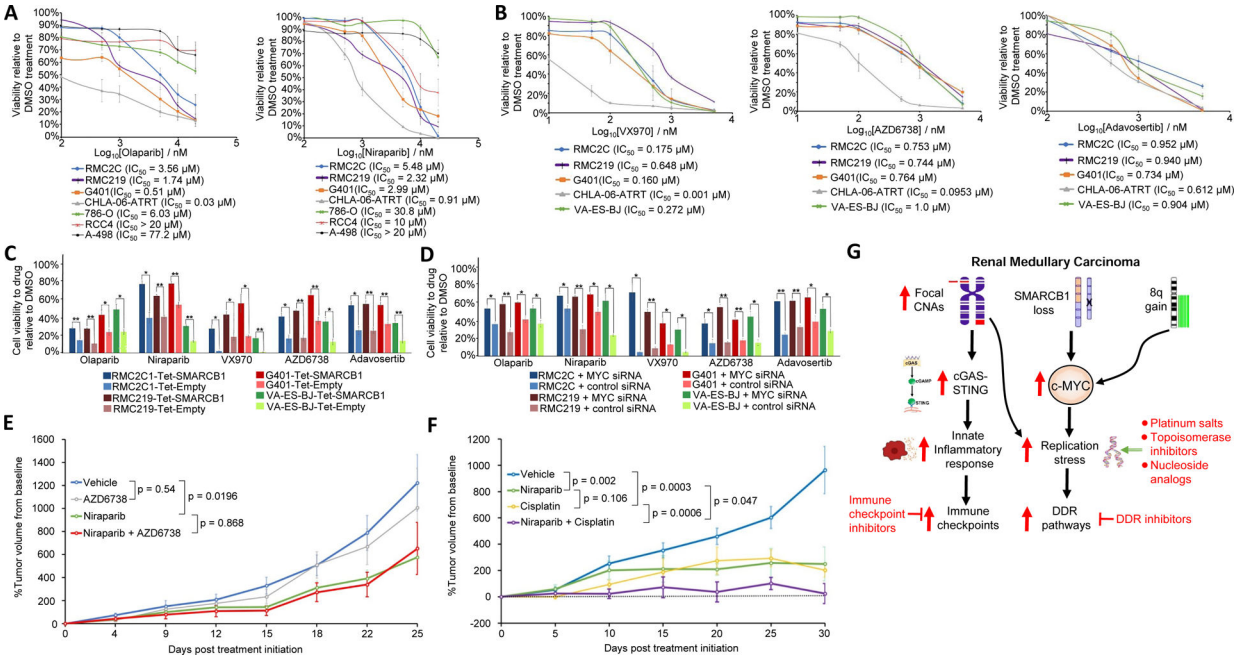

Figure 7: RMC is Vulnerable to Drugs Targeting Replication Stress *In Vitro* and *In Vivo*

(A) Viability curves and half maximal inhibitory concentrations (IC_{50}) of SMARCB1-negative (RMC2C, RMC219, G401, CHLA-06-ATRT) and SMARCB1-positive (786-O, RCC4, A-498) cell lines after 120-hour exposure to the PARP inhibitors olaparib and niraparib. **(B)** Viability curves and IC50 of SMARCB1-negative cell lines after exposure to the ATR inhibitors VX970 and AZD6738 and to the WEE1 inhibitor adavosertib. **(C & D)** Viability of RMC2C, RMC219, G401, and VA-ES-BJ cells expressing doxycycline-induced SMARCB1 or empty vector control **(C)** or treated with siRNA against c-MYC or sham control **(D)** followed by 120-hour exposure to olaparib (10 μM), niraparib (10 μM), VX970 (1 μM), AZD6738 (1 μM), or adavosertib (1 μM). * $p < 0.05$, ** $p < 0.01$ by unpaired two-tailed Welch's t-test. All results in **A-D** are presented as means ± SEM from triplicates. **(E)** *In vivo* antitumor effect of niraparib, AZD6738, and their combination in the RMC2X PDX mouse model (n=5 mice / group). Plots represent mean percentage tumor volume change from baseline ± SEM. **(F)** *In vivo* antitumor effect of cisplatin alone or in combination with niraparib in RMC tumors (n=10 mice / group). Plots represent mean percentage tumor volume change from baseline ± SEM. **(G)** Schematic model of the interplay between SMARCB1 loss and CNAs in inducing replication stress and inflammatory responses in RMC. Loss of SMARCB1 and gain of 8q promote MYC-induced replication stress which renders RMC cells susceptible to DNA damaging agents such as platinum salts, topoisomerase inhibitors, and nucleoside analogs. DNA damage repair (DDR) pathways induced by replication stress can be directly targeted by DDR inhibitors. The inflammatory responses activated via cGAS-STING signaling in RMC upregulate immune checkpoints that can be therapeutically targeted. See also Figure S7 and Table S7.

KEY RESOURCES TABLE

REAGENT or RESOURCE	SOURCE	IDENTIFIER
Antibodies		
Mouse monoclonal anti-BAF47 (anti-SMARCB1) Clone 25	BD Biosciences	Cat# 612111; RRID: AB_2191717
Mouse monoclonal anti-INI1/SNF5 (anti-SMARCB1) antibody clone 2C2	Sigma-Aldrich	Cat# SAB4200202; RRID: AB_10697389
Rabbit polyclonal anti-phospho-Histone H2A.X at serine 139	Cell Signaling Technology	Cat# 2577; RRID: AB_2118010
Mouse monoclonal anti-c-MYC antibody 9E10	Santa Cruz Biotechnology	Cat# sc-40; RRID: AB_627268
Rabbit polyclonal anti-PARP	Cell Signaling Technology	Cat# 9542; RRID: AB_2160739
Goat polyclonal anti-ATR	Santa Cruz Biotechnology	Cat# sc-1887; RRID: AB_630893
Rabbit polyclonal anti-phospho-ATR at serine 428	Cell Signaling Technology	Cat# 2853; RRID: AB_2290281
Mouse monoclonal anti-TP53	Santa Cruz Biotechnology	Cat# sc-126; RRID: AB_628082
Rabbit polyclonal anti-phospho-TP53 at serine 15	Cell Signaling Technology	Cat# 9284; RRID: AB_331464
Mouse monoclonal anti-actin	Santa Cruz Biotechnology	Cat# sc-47778 HRP; RRID: AB_2714189
Rabbit polyclonal anti-phospho-CDK1 at tyrosine 15	Cell Signaling Technology	Cat# 9111; RRID:AB_331460
Mouse monoclonal anti-RPA 32 kDa subunit 9H8	Santa Cruz Biotechnology	Cat# sc-56770; RRID: AB_785534
Rabbit polyclonal anti-phospho-RPA32 at serines 4 and 8	Bethyl	Cat# A300–245A; RRID: AB_210547
Mouse monoclonal anti-FANCD2	Santa Cruz Biotechnology	Cat# sc-20022; RRID: AB_2278211
Rabbit polyclonal anti-PBRM1	Bethyl	Cat# A301–591A; RRID: AB_1078808
Rabbit monoclonal anti-BRG1 (anti-SMARCA4)	Abcam	Cat# ab110641; RRID: AB_10861578
Mouse monoclonal anti-BAF250a (anti-ARID1A)	Santa Cruz Biotechnology	Cat# sc-32761; RRID: AB_673396
Anti-rabbit IgG-HRP	Rockland	Cat# 88-8886-31; RRID: AB_2614893
Anti-mouse IgG-HRP	Rockland	Cat# 18-8817-30; RRID: AB_2610849
Rabbit monoclonal anti-STING	Cell Signaling Technology	Cat# 13647; RRID: AB_2732796
Rabbit polyclonal anti-CD3	Agilent	Cat# A0452; RRID: AB_2335677
Mouse monoclonal anti-CD4	Leica Biosystems	Cat# NCL-L-CD4–368; RRID: AB_563559
Mouse monoclonal anti-CD8	Thermo Fisher Scientific	Cat# MS-457-S; RRID: AB_61027
Mouse monoclonal anti-FOXP3	BioLegend	Cat# 320102; RRID: AB_430881
Mouse monoclonal anti-CD20	Agilent	Cat# M0755; RRID: AB_2282030
Mouse monoclonal anti-CD68	Agilent	Cat# M0876; RRID: AB_2074844
Rabbit monoclonal anti-PD-L1	Cell Signaling Technology	Cat# 13684; RRID: AB_2687655
Rabbit monoclonal anti-PD-1	Abcam	Cat# AB201825; RRID:AB_2728811
Rabbit polyclonal anti-c-MYC	Santa Cruz Biotechnology	Cat# sc-764; RRID: AB_631276
Rabbit Normal IgG Control Antibody	Cell Signaling Technology	Cat# 2729; RRID: AB_1031062

REAGENT or RESOURCE	SOURCE	IDENTIFIER
Mouse monoclonal anti-IdU / anti-BrdU clone B44	BD Biosciences	Cat# B44; RRID: AB_2313824
Rat monoclonoal anti-CldU / anti-BrdU (BU1/75 ICR1)	Santa Cruz Biotechnology	Cat# sc-56258, RRID: AB_781696
Goat polyclonal anti-mouse Alexa Fluor 488	Thermo Fisher Scientific	Cat# A-11001; RRID: AB_2534069
Goat polyclonal anti-rat Alexa Fluor 555	Thermo Fisher Scientific	Cat# A-21434; RRID: AB_2535855
Bacterial and Virus Strains		
E.coli DH5α	Invitrogen	Cat#18265017
Biological Samples		
Renal medullary carcinoma tumor samples	UTMDACC Department of Genitourinary Medical Oncology	N/A
Normal adjacent kidney	UTMDACC Department of Genitourinary Medical Oncology	N/A
Collecting duct carcinoma tumor samples	UTMDACC Department of Genitourinary Medical Oncology	N/A
Upper tract urothelial carcinoma tumor samples	UTMDACC Department of Genitourinary Medical Oncology	N/A
Malignant rhabdoid tumor FFPE slides	Dolores Lopez-Terrada (dhterrad@texaschildrenshospital.org)	N/A
Chemicals, Peptides, and Recombinant Proteins		
Doxycycline	Thermo Fisher Scientific	Cat# BP26531; CAS: 10592-13-9
Olaparib (AZD2281)	Selleckchem	Cat# S1060; CAS: 763113-22-0
Niraparib (MK-4827)	Selleckchem	Cat# S2741; CAS: 1038915-60-4
Berzosertib (VX970)	Selleckchem	Cat# S7102; CAS: 1232416–25-9
Ceralasertib (AZD6738)	Selleckchem	Cat# S7693; CAS: 1352226-88-0
Adavosertib (MK-1775)	Selleckchem	Cat# S1525; CAS: 955365-80-7
Doxorubicin	UTMDACC Department of Pharmacy	CAS: 23214-92-8
Gemcitabine	UTMDACC Department of Pharmacy	CAS: 95058-81-4
Carboplatin	UTMDACC Department of Pharmacy	CAS: 41575-94-4
Cisplatin	UTMDACC Department of Pharmacy	CAS: 15663-27-1
Paclitaxel	UTMDACC Department of Pharmacy	CAS: 33069-62-4
Critical Commercial Assays		
Universal Mycoplasma Detection Kit	ATCC	Cat#30-1012K
QIAamp DNA FFPE Tissue Kit (50)	Qiagen	Cat#56404
AllPrep DNA/RNA Mini Kit (50)	Qiagen	Cat#80204
SureSelectXT Reagent Kit	Agilent	Cat#G9612B
4200 TapeStation High Sensitivity D1000 ScreenTape	Agilent	Cat#5067-5584
Qubit dsDNA HS Assay Kit	Thermo Fisher Scientific	Cat#Q32851
KAPA Library Quantification Kit	Roche	Cat#KK4824
FoundationOne CDx	Foundation Medicine	F1CDX
Oligonucleotide Array-Based CGH for Genomic DNA Analysis	Agilent	Protocol # G4410-90010

REAGENT or RESOURCE	SOURCE	IDENTIFIER
RNeasy Mini Kit (250)	Qiagen	Cat#74106
Infinium HumanMethylation450 (HM450) BeadChip array	Illumina	Cat#WG-314-1002
EZ DNA methylation kit	Zymo Research	Cat#D5001
SMARCB1BA-20-GROR Break Apart FISH Probe	Empire Genomics	Cat#SMARCB1BA-20-GROR
SALSA MLPA P258 (SMARCB1) kit	MRC-Holland	Cat#P258-050R
HiSKY Probe Kit	Applied Spectral Imaging	Cat#FPRPR0028
siGENOME Human MYC siRNA SMARTpool	Horizon Discovery	Cat#M-003282-07-0010
siGENOME Non-targetin siRNA control pool	Horizon Discovery	Cat# D-001206-13-20
Cell Proliferation Kit I (MTT)	Sigma-Aldrich	Cat#11 465 007 001
Deposited Data		
Raw RMC sequencing data	This paper	NCBI Sequence Read Archive (SRA) accession: PRJNA605003 ; https://www.ncbi.nlm.nih.gov/sra/PRJNA605003
Clear cell renal cell carcinoma sequencing data	TCGA; Cancer Genome Atlas Research, 2013	https://portal.gdc.cancer.gov/projects/TCGA-KIRC
Papillary renal cell carcinoma sequencing data	TCGA; Cancer Genome Atlas Research et al., 2016	https://portal.gdc.cancer.gov/projects/TCGA-KIRP
Chromophobe renal cell carcinoma sequencing data	TCGA; Davis et al., 2014	https://portal.gdc.cancer.gov/projects/TCGA-KICH
Kidney MRT sequencing data	Chun et al., 2016	http://target.nci.nih.gov/dataMatrix/TARGET_DataMatrix.html
MRT and ATRT sequencing data	Lee et al., 2012	dbGaP accession no. phs000508
G401 c-MYC ChiP-seq data	Weissmiller et al., 2019	GEO: GSE109310
Experimental Models: Cell Lines		
HEK-293FT	Thermo Fisher Scientific	Cat# R70007, RRID: CVCL_6911
G401	ATCC	Cat#CRL-1441, RRID: CVCL_0270
CHLA-06-ATRT	ATCC	Cat#CRL-3038, RRID: CVCL_AQ42
VA-ES-BJ	ATCC	Cat#CRL-2138, RRID: CVCL_1785
A-498	ATCC	Cat#CRL-7908, RRID: CVCL_1056
786-O	ATCC	Cat#CRL-1932, RRID: CVCL_1051
RCC4	ECACC	Cat#03112702, RRID: CVCL_UY81
RMC2C	This paper	N/A
RMC219 (JHRCC219)	Dong et al., 2017 Emily H. Cheng (ChengE1@mskcc.org)	N/A
RMC2C1-Tet-Empty	This paper	N/A
RMC2C1-Tet-SMARCB1	This paper	N/A
RMC219-Tet-Empty	This paper	N/A
RMC219-Tet-SMARCB1	This paper	N/A
G401-Tet-Empty	This paper	N/A
G401-Tet-SMARCB1	This paper	N/A

REAGENT or RESOURCE	SOURCE	IDENTIFIER
VA-ES-BJ-Tet-Empty	This paper	N/A
VA-ES-BJ-Tet-SMARCB1	This paper	N/A
HEK293-control gRNA	This paper	N/A
HEK293-SMARCB1-KO	This paper	N/A
Experimental Models: Organisms/Strains		
Mouse: CB17/lcr-Prkd^{scid}/lcrlcoCrl	Charles River	Cat#236; RRID: IMSR_CRL:561
Mouse: RMC2X patient-derived xenograft	This paper; Jose A. Karam (JAKaram@mdanderson.org) and Christopher G. Wood (cgwood@mdanderson.org)	N/A
Oligonucleotides		
SMARCB1 gRNA (1): TGAGAACGCATCTCAGCCCG	GenScript	https://www.genscript.com/gRNA-detail/6598/SMARCB1-CRISPR-guide-RNA.html
SMARCB1 gRNA (2): CATCGATCTCCATGTCCAGC	GenScript	https://www.genscript.com/gRNA-detail/6598/SMARCB1-CRISPR-guide-RNA.html
Non-targeting control gRNA sequence: GGGACGCGAAAGAAACCAGT	John Doench & David Root	Addgene plasmid # 80196; RRID: Addgene_80196
CCNE2 TSS primer forward: CAGCACAACGTGGAGTGG	This paper	N/A
CCNE2 TSS primer reverse: AGAGCAGAGCCGCACTTG	This paper	N/A
CDK4 TSS primer forward: ATGTGACCAGCTGCCAAAG	This paper	N/A
CDK4 TSS primer reverse: TTACACTCTTCGCCCTCCTC	This paper	N/A
ATF4 TSS primer forward: CGAAGGAAAGAACGGACTCTG	This paper	N/A
ATF4 TSS primer reverse: TTATGGCCTCACGAAAGGAG	This paper	N/A
PRM1 TSS primer forward: ACAGAGCGACACCCTGTCAT	This paper	N/A
PRM1 TSS primer reverse: AGGCGGTGGTTACACAACAT	This paper	N/A
Recombinant DNA		
pIND20-fSNF5-HA vector	Bernard E. Weissman; Wei et al., 2014	N/A
pInducer20 empty backbone	Stephen Elledge	Addgene plasmid # 44012; RRID: Addgene_44012
pLentiCRISPR v2 anti-SMARCB1 gRNA	GenScript	https://www.genscript.com/gRNA-detail/6598/SMARCB1-CRISPR-guide-RNA.html
psPAX2	Didier Trono	Addgene plasmid # 12260; RRID: Addgene_12260
pMD2.G	Didier Trono	Addgene plasmid # 12259; RRID: Addgene_12259
pLentiCRISPR v2 non-targeting control gRNA	John Doench & David Root	Addgene plasmid # 80196; RRID: Addgene_80196
Software and Algorithms		
R statistical package	R Core Team, 2019	http://www.r-project.org/

REAGENT or RESOURCE	SOURCE	IDENTIFIER
rms	Harrell, 2015	https://github.com/harrelfe/rms
Hmisc	Harrell, 2015	https://github.com/harrelfe/Hmisc
DAVID Bioinformatics resources database (v6.8)	Huang da et al., 2009a; Huang da et al., 2009b	https://david.ncifcrf.gov/
Gene set enrichment Analysis	Subramanian et al., 2005	http://software.broadinstitute.org/gsea/index.jsp
MOSAIK alignment software	Lee et al., 2014	https://github.com/wanpinglee/MOSAIK
GigaBayes/FreeBayes	Marth et al., 1999	https://github.com/ekg/freebayes
SIFT	Vaser et al., 2016	http://sift-dna.org/sift4g
Mutational signature database	Sanger Institute Alexandrov et al., 2013	https://cancer.sanger.ac.uk/cosmic/signatures
BSgenome.Hsapiens.UCSC.hg19 (version:1.4.0)	The Bioconductor Dev Team, 2014	http://bioconductor.org/packages/release/data/annotation/html/BSgenome.Hsapiens.UCSC.hg19.html
VirusSeq	Chen et al., 2013	http://odin.mdacc.tmc.edu/~xsu1/VirusSeq.html
ExomeCN	Zhang et al., 2014	MD Anderson Cancer Cent in-house software
Sequenza	Favero et al., 2015	https://github.com/cran/sequenza
GISTIC2.0	Mermel et al., 2011; Beroukhim et al., 2010	http://portals.broadinstitute.org/cgi-bin/cancer/publications/pub_paper.cgi?mode=view&paper_id=216&p=t
hg19 cytoband coordinates	Genome Reference Consortium	http://hgdownload.cse.ucsc.edu/goldenpath/hg19/database
Feature-Extraction V9.1.3	Agilent	https://www.agilent.com/en/promotions/release-note-feature-extraction-software-version-9-1-3
GENCODE annotation	Harrow et al., 2012	https://www.gencodegenes.org/
HTSeq	Anders et al., 2015	https://github.com/simon-anders/htseq
DESeq2	Love et al., 2014	https://github.com/mikelove/DESeq2
Molecular Signatures Database (MSigDB)	Subramanian et al., 2005; Liberzon et al., 2015	http://software.broadinstitute.org/gsea/msigdb/collections.jsp
MCP-counter 1.1.0	Becht et al., 2016	https://omictools.com/mcp-counter-tool
minfi	Aryee et al., 2014	https://github.com/hansenlab/minfi
HiBand	Applied Spectral Imaging	https://spectral-imaging.com/products/hiband/
ImageJ	NIH Schneider et al., 2012	https://imagej.nih.gov/ij/
FindFoci	Herbert et al., 2014	https://github.com/aherbert/gdsc
bowtie2	Langmead and Salzberg, 2012	https://github.com/BenLangmead/bowtie2
Integrative Genome Viewer	Thorvaldsdottir et al., 2013	https://software.broadinstitute.org/software/igv/
MACS2	Zhang et al., 2008	https://github.com/taoliu/MACS
BEDTOOLS	Quinlan and Hall, 2010	https://github.com/ryanlayer/bedtools
Hallmark pathways	Liberzon et al., 2015	https://www.gsea-msigdb.org/gsea/msigdb/collections.jsp
REACTOME pathways	Fabregat et al., 2018	https://www.gsea-msigdb.org/gsea/msigdb/collections.jsp

REAGENT or RESOURCE	SOURCE	IDENTIFIER
Dr Fit	Di Veroli et al., 2015	https://sourceforge.net/projects/drfit/
Other		
Sensitivity of human cell lines to olaparib	Genomics of Drug Sensitivity in Cancer database	https://www.cancerrxgene.org/translation/Drug